A Force-Detection NMR Sensor in CMOS-MEMS

by
Kevin M. Frederick

Bachelor of Science, 2001
Carnegie Mellon University, Pittsburgh, Pennsylvania

A report submitted in partial fulfillment of the requirements for the degree of:

MASTER OF SCIENCE

in

ELECTRICAL AND COMPUTER ENGINEERING

at

CARNEGIE MELLON UNIVERSITY

Thesis Committee Members:
Advisor: Professor Gary K. Fedder
Reader: Professor David N. Lambeth

2003

Abstract

Nuclear Magnetic Resonance (NMR) on micro-liter samples using the Force Detection NMR (FDNMR) method will enable mobile and embedded detection of many elements without a multi-tesla superconducting magnet. This report presents a FDNMR sensor which has the ability to detect hydrogen of a 0.52 μL water sample in a 1 tesla magnetic field. The sensor is a micromachined cantilevered paddle within a CMOS chip measuring 2.5 mm x 2.5 mm x 540 μm with integrated amplification electronics.

To begin the paddle fabrication, a 30 μm thick silicon membrane with a thin layer of CMOS interconnect on top, is made by Deep Reactive Ion Etching (DRIE) the backside of the chip. The backside area is patterned with photoresist and etched into many close-proximity, slightly undercut high-aspect-ratio trenches to achieve a uniform membrane thickness. The resulting membrane measures 1370 μm by 1850 μm, with center to edge thickness variations less than 5 μm. A 0.6 mm x 0.6 mm x 0.25 mm piece of pure nickel is glued to the etched membrane surface as a detector magnet. Freon plasma etches trenches into the silicon dioxide interconnect layer not masked by aluminum, and a final DRIE extends the trenches through the silicon membrane. The final etch releases the folded-mass cantilever with 1 mm long spring beams and a 1.1 mm^2 paddle surrounded by a capacitive bridge sensor to measure vertical displacement.

Integrated electronics drive the input and amplify the output of the balanced capacitive bridge which is made of lateral air gap capacitors between interdigitated micromechanical fingers. Force induced vertical cantilever displacement imbalances the bridge and the amplified output signal is measured by external test equipment. The bridge has the dynamic range to measure up to ±0.5 μm displacement at the maximum sensitivity of 5.12 mV/nm and up to ±2.0 μm with less sensitivity.

The FDNMR sensor is tested in response to electrostatic, mechanical, acceleration, and magnetic forces. The cantilevered paddle at 760 Torr resonates at 3.6 kHz (Q = 20) compared to 3.0 kHz (Q = 430) by simulation. The bridge output amplitude is linear with oscillating magnetic force amplitude. Estimated noise bandwidth is extracted from time-domain averaging of experimental data. Assuming a 1 MHz system bandwidth, 512 measurements equal a 1.95 kHz noise bandwidth and a 2.4 Å displacement noise floor with an SNR of 1. This displacement corresponds to a 4.4 pN oscillating force at 2.5 mTorr. A 100 Hz noise bandwidth will detect the 1.0 pN FDNMR force from a 0.52 μL water sample in a 1 tesla magnetic field.

Table of Contents

I. Introduction

Nuclear magnetic resonance (NMR) is a property of many materials when immersed in a strong, constant, and orthogonal magnetic field, $\vec{B}_0$, and excited by an oscillating magnetic field, $\vec{B}_1$ [9, 17]. Elements and molecules of a sample can be detected and classified by their response to this excitation. The sample NMR frequency and amplitude are directly proportional to the magnitude of the $\vec{B}_0$ field and the volume of the sample, respectively. The $\vec{B}_0$ field strengths for NMR experiments are typically greater than two tesla (T) and are created by large superconducting electromagnets. Sample sizes are typically milliliters for bulk detection and liters for imaging. The sample size has practical limits constrained by the overall system size needed to maintain a uniform $\vec{B}_0$ field across the sample. Theory predicts that reduced sample size and field strength allow use of a permanent magnet to supply the uniform $\vec{B}_0$ field and thereby enable construction of a miniature NMR system [11]. This report presents a new implementation of the critical sensor in a miniature NMR system. The sensor is designed to detect the NMR of a 1 microliter (μL) scale sample in a sub-tesla $\vec{B}_0$ field. A NMR system with this sensor has application in detecting chlorine concentrations dangerous to steel reinforcement in the concrete of bridge decks. Early detection allows preemptive action to delay and even prevent expensive and disruptive replacement of infrastructure [18].

The objective of this work is to demonstrate a Force Detection NMR (FDNMR) sensor which couples the oscillating magnetic moment of a concrete sample experiencing NMR to a mechanically resonant micro-cantilever [30]. The sensor is a silicon chip fabricated with Complementary-Metal-Oxide-Semiconductor (CMOS) electronics technology to exploit the capability to co-locate sensor electronics with the resonant transducer [36]. The induced cantilever motion from the sample NMR is detected with a capacitive sensor designed into the cantilever on the chip [37]. On-chip amplification electronics convert the capacitive sensor output into a robust voltage for external measurement and analysis [23]. This report provides a background on NMR physics and the design, fabrication, and test details of the completed chip. Experimental demonstration the FDNMR sensor detecting a sample experiencing NMR is not part of this report.

a. Motivation for Micro-NMR

The miniaturization of NMR technology (Micro-NMR) can open major new applications. Most current commercial NMR systems focus on large-scale medical imaging of human appendages and entire bodies [19], though small-scale bench top systems are emerging in the marketplace [29]. The large systems occupy whole rooms in hospitals and are completely immobile. The tremendous size comes from the use of superconducting coils to generate the 1.5 T and 3 T $\vec{B}_0$ fields necessary in common Magnetic Resonance Imaging (MRI) systems. These systems can create three-dimensional images from NMR signal properties for any sensitive sample. The coils require extensive thermal control to safely maintain a large current carrying capacity, while consuming minimal power. The coils must also be large to maintain the 1ppm field homogeneity across tens of centimeters in 3 dimensions, critical for modern high-resolution MRI of humans. As a specific example, a 2.35 T $\vec{B}_0$ system measures approximately 1.5 m on a side with a 78 cm^2 cylinder bore (10 cm diameter) for sample analysis [18, 38]. The high homogeneity and strength of the $\vec{B}_0$ field in this system provides spatial imaging with 1 mm resolution.

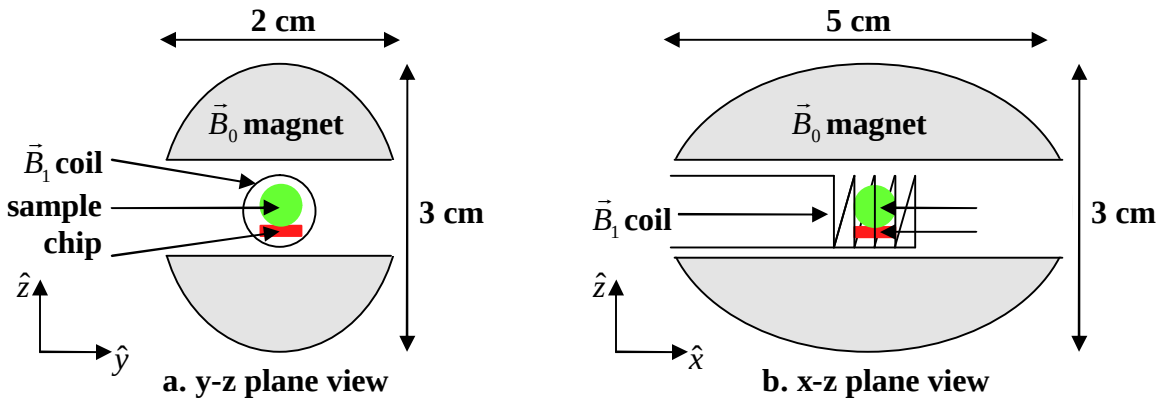

Figure I.1 Micro-NMR System

The Micro-NMR system considered in this report and outlined in Figure I.1 is designed to detect the presence and quantity of much smaller samples. The small sample size dictates the size and shape of the magnet necessary to maintain a homogeneous magnetic field across the entire sample. High speed and fine spatial resolution are not goals of the system, so the $\vec{B}_0$ field strength can be lowered to 0.5 T. Machined permanent magnets, which can sustain the 0.5 T field strength, complete the system without needing thermal

management. The decrease in NMR signal generated by the small sample and the low $\vec{B}_0$ field strength is compensated by using a detection method less sensitive to these criteria, by limiting the measurement bandwidth, and by co-locating signal amplification electronics with the sensor on the chip.

A Micro-NMR system has advantages for both biological and infrastructure applications. Biological applications may have only very small samples available for analysis. Examples include biological fluids and cell clusters. A limited sample must often be shared among several tests, as in hazardous biochemical material analysis applications. The compact size of the permanent magnet and micro-chip sensor allows the complete system to be mobile or embedded. The system can be easily transported to a test site. As the ultimate application, many systems could be properly packaged and set in the wet concrete mix of a structure as it is constructed. Radio or wired communication to the systems could then record the presence and quantity of water and chlorine in the concrete near the systems. With systems in strategic locations inside an infrastructure, its condition could be rapidly diagnosed without removing any structural cores for laboratory analysis.

b. Micro-Sensor Topologies

Two types of systems, conceptually illustrated in Figure I.2, can detect the NMR of small samples in a low magnetic field. Induction Detection NMR (IDNMR) is one option and is the method used in medical imaging systems and in conventional NMR analysis systems. In the IDNMR method, sample magnetic resonance continues for a period of time after external excitation has stopped. A sinusoidal voltage, V_0, is detected across a pickup coil when excited by the decaying NMR of a sample [28]. The transverse pickup coil axis is orthogonal to $\vec{B}_0$, and along $\vec{B}_1$, as in Figure I.2a.

Force Detection NMR (FDNMR) is a recent detection method, which relies on measuring the induced motion of a cantilever [32]. A specific type of NMR, adiabatic rapid passage (ARP), causes the magnetic moment of a sample to oscillate parallel to $\vec{B}_0$ [30]. The oscillating magnetic moment creates an oscillating field gradient along the $\vec{B}_0$ field direction. The field gradient exerts a force, $\vec{F}_m$, on the magnet and its attached micro-cantilever in Figure I.2b, at the mechanical resonant frequency.

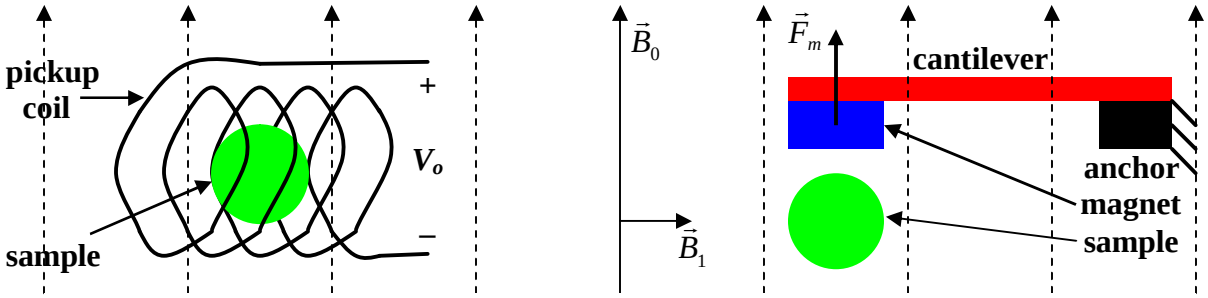

Figure I.2 Basic NMR Sensor Schematics

The FDNMR method is chosen to implement a Micro-NMR sensor for four reasons. First, the Signal-to-Noise Ratio (SNR) of FDNMR is linearly proportional to $\vec{B}_0$, while IDNMR has a SNR proportional to $\left|\vec{B}_0\right|^2$ ($\left|\vec{B}_0\right|^{7/4}$ at high magnetic fields and with thin coil wires) [11]. This scaling clearly favors FDNMR at low field strengths. Second, the detectable FDNMR signal coupled to the cantilever is at a different frequency from the NMR excitation frequency, so excitation and detection can be performed concurrently. The constant acquisition of data avoids the time necessary in IDNMR to re-excite the sample after its signal decays. Since the SNR $\propto \sqrt{N}$, where N is the number or duration of detection sequences, constant data acquisition can greatly reduce the total time necessary to improve the low SNR of small samples. Third, a specific topology of FDNMR, known as BOOMERANG and developed at the California Institute of Technology, allows an entire sample to contribute to the signal as it does in IDNMR [24]. FDNMR without BOOMERANG causes a $\vec{B}_0$ gradient across the sample, limiting the material at resonance to a thin slice of the sample [8]. Fourth, FDNMR is a new approach to NMR. Thus it is a novel measurement technique without experimentally demonstrated limits of detection.

c. FDNMR-on-a-Chip System Overview

The physical FDNMR sensor in Figure I.3 is composed of a micro-machined resonant cantilever in a CMOS silicon chip with a small disk of ferromagnetic material attached to the cantilever. The chip includes a 5 μm thick top layer of circuits, a 535 μm thick silicon substrate, and measures 2.5 mm on a side. The cantilever integrated into the chip is a large paddle suspended by two spring beams. The paddle measures 1.1 mm by 1.0 mm to easily accommodate the magnet, which is a disc approximately 250 μm thick and 750 μm

in diameter. This magnet provides the coupling mechanism between the oscillating magnetic moment of the NMR sample and the mechanical cantilever. The complete sensor dimensions are chosen to match a 0.52 μL (500 μm radius) spherical sample, since simulations demonstrate that the SNR of FDNMR is equal to or better than IDNMR on samples of hydrogen atoms in water at this size [11]. This size is also convenient for micro-fabrication. The mechanically active cantilever with integrated displacement sensitive capacitors, amplification electronics, and bond pads fit easily within the 2.5 mm by 2.5 mm chip area.

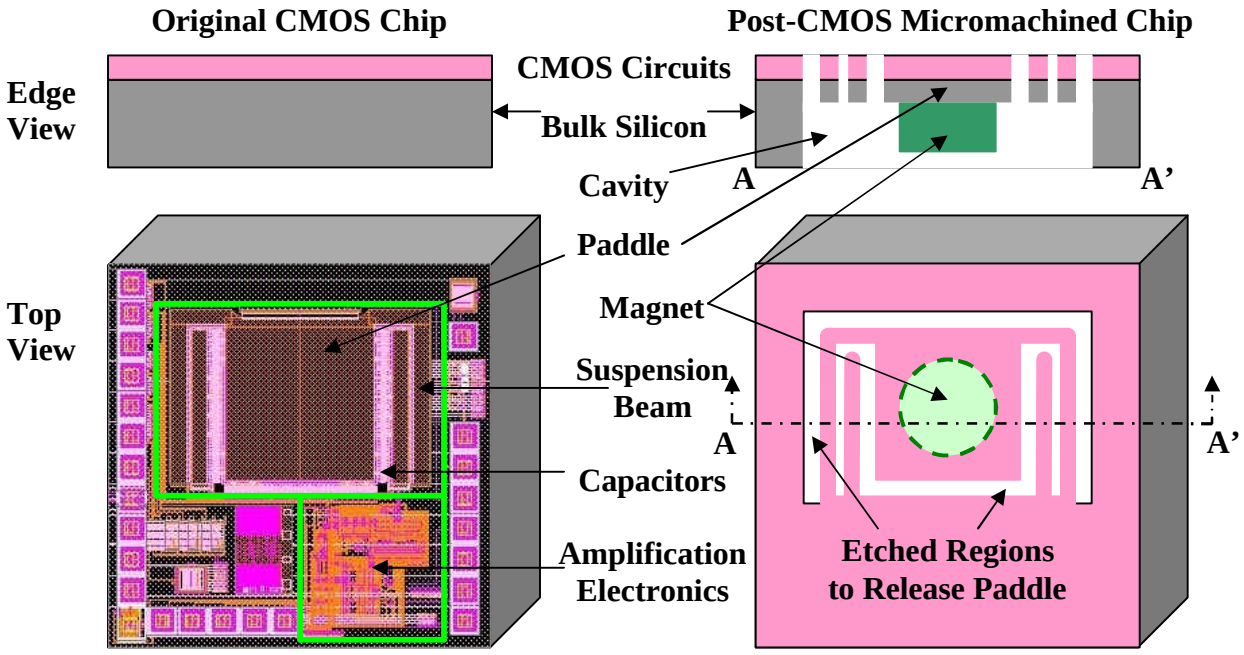

Figure I.3 FDNMR-on-a-Chip System Overview

The CMOS electronics fabrication was completed by the Austria MicroSystems (AMS) foundry, in a process similar to those offered by the Metal-Oxide-Semiconductor Implementation Service (MOSIS) [2, 26]. The chip from the foundry has embedded transistor circuits and three layers of aluminum interconnect on the topside of the silicon substrate. This chip is post-CMOS processed in several stages specifically for this work. The backside (no circuits) is etched to form a cavity in the silicon below the cantilever assembly [36]. A small disc of pure nickel is attached to the backside of the cavity as the magnet and then the topside of the chip is etched to define and release the cantilever assembly from the surrounding silicon substrate. This allows the paddle, with attached magnet, to move normal to the plane of the chip surface. Finally, the backside of the chip is mounted to a thin glass cover-slip to separate the nickel magnet from NMR samples.

This assembly is placed in a ceramic package and the electrical contact bond-pads of the chip are wire-bonded to the package for external access and testing. In the final package, shown in Figure I.4, a cap is sealed over the wire-bonded chip. A tube protrudes from the chip chamber allowing vacuum pumping of the chamber. A vacuum in the chamber eliminates viscous air damping and molecular impingement on the cantilever, resulting in a higher quality mechanical resonance and enhanced cantilever motion from a given force [34].

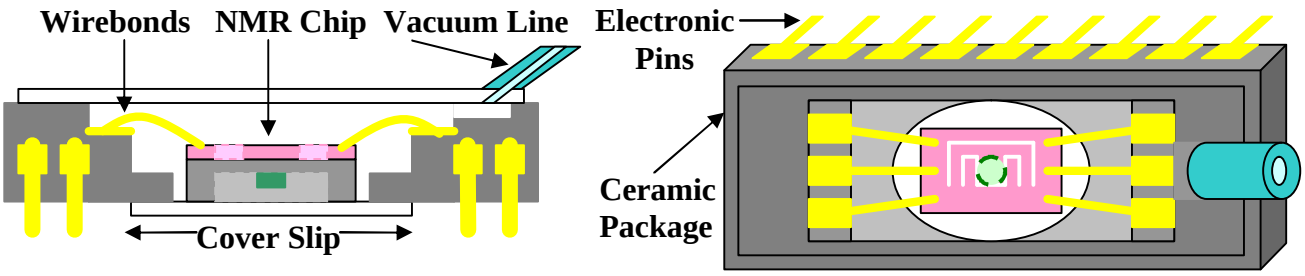

Figure I.4 FDNMR Sensor Packaging, side view and top view

The sensor has a capacitive bridge surrounding the paddle to detect its vertical motion. A constant voltage is applied across the capacitive bridge, generating a non-zero but small sense voltage when the cantilever is vertically misaligned from the chip surface [37]. On-chip electronics then amplify the sense voltage to allow external measurement without loading the displacement sensitive capacitive bridge [23]. The amplifier output voltage changes linearly with vertical cantilever displacement. Resonant cantilever motion is reported as a sinusoidal voltage waveform.

This work demonstrates the complete post-CMOS fabrication of the FDNMR sensor. Several chips are etched to form silicon cantilevers 60 μm and 30 μm thick. Nickel is attached as the detector magnet. The cantilevers and integrated capacitive bridges are released. The capacitors successfully measure both static displacement and dynamic motion of the cantilever. The sensor is excited by physical probing, electrostatic force, inertial force, and magnetic force. With these sensing modes confirmed, the packaged sensor can be integrated with a sample, an excitation coil to provide a $\vec{B}_1$ field, and a homogeneous $\vec{B}_0$ field into a system to determine its NMR detection capabilities. The system integration and the related testing is left as future work.

II. NMR Background

NMR is used to detect the presence and quantity of a specific element or molecule in a sample of material. This section provides a brief synopsis of the atomic origin and physical forces involved in NMR, with a focus on FDNMR. A quantitative comparison between the SNR of IDNMR and FDNMR demonstrates the feasibility of using FDNMR to detect 1 μL scale hydrogen samples.

a. The NMR Property of Atoms

Nuclear magnetic resonance is the cyclic motion of the nuclear moment of an atomic nucleus in response to both a strong constant magnetic field and a weaker but sinusoidally oscillating magnetic field, orthogonal to the strong field. Edward Purcell and Felix Bloch independently discovered the phenomenon in 1945 [20]. To have a nuclear moment, $\vec{m}_s$, an atom must have a property called nuclear spin, representing the angular momentum of the atomic nucleus. An atomic nucleus has nuclear spin when the number of protons or neutrons is odd or they are not equal. Each spin configuration of the imbalanced nuclear particles leads to a spin state of the atom. For example, an odd atomic mass allows an nuclear moment to have an even number of spin states. Each spin state represents a specific energy level a nuclear moment can occupy. The energy separation between states, ΔE, is given by

$$\Delta E = \hbar g \left|\vec{B}_0\right| \tag{2.1}$$

where h is Planck's constant divided by 2π, $1.055*10^{-34}$ J-s/rad, g is the gyromagnetic ratio of the atom, and $\left|\vec{B}_0\right|$ is the magnitude of the applied DC magnetic field permeating the sample. The gyromagnetic ratio is unique to a given atom and is $2.675*10^{8}$ rad/(T-s) for hydrogen and $2.621*10^{7}$ rad/(T-s) for chlorine.

Any sample is made up of an enormous number of atoms, each with an individual nuclear moment. For example, a 1 μL sample of water contains $6.69*10^{19}$ hydrogen atoms, each with an average nuclear moment of 2.79 nuclear magnetrons ($\vec{m}_s$ = $1.41*10^{-26}$ J/tesla). When the water sample is placed in a 1 T $\vec{B}_0$ field, the nuclear moments behave as individual magnetic dipoles and align to the field with an average energy of $1.41*10^{-26}$ J. At room temperature, 300 K, $4.16*10^{-21}$ J phonons from lattice vibrations also interact with the nuclear moments and cause most of them to become randomly oriented. Approximately 1 in 1000 of

the nuclear moments will have the energy to remain aligned to the $\vec{B}_0$ field. All the aligned nuclear moments move together to form the vector sum $\vec{M}_s$, the magnetization of the entire sample. The randomly oriented nuclear moments do not contribute to $\vec{M}_s$. To explain the behavior of $\vec{M}_s$ in the magnetic fields of NMR, consider the behavior of an individual nuclear moment, $\vec{m}_s$, during the NMR excitation in Figure II.1.

The $\vec{B}_0$ field induces a force on $\vec{m}_s$ to cause a time dependency as,

$$\frac{\partial \vec{m}_s}{\partial t} = g\vec{m}_s \, x \, \vec{B}_0 \tag{2.2}$$

and the nuclear moment, $\vec{m}_s$, possesses an energy, *E*, where

$$E \propto -(\vec{m}_s \bullet \vec{B}_0) \tag{2.3}$$

Equation 2.3 dictates that the nuclear moment is at a minimum energy configuration when $\vec{m}_s$ and $\vec{B}_0$ are aligned. However, from Equation 2.2, $\vec{m}_s$ always precesses around $\vec{B}_0$. This is illustrated in Figure II.1a where $\vec{B}_0$ is along the $\hat{z}$ axis and $\vec{m}_s$ precesses about $\vec{B}_0$ at the Larmor Frequency, w_0, where

$$w_0 = g\left|\vec{B}_0\right| \tag{2.4}$$

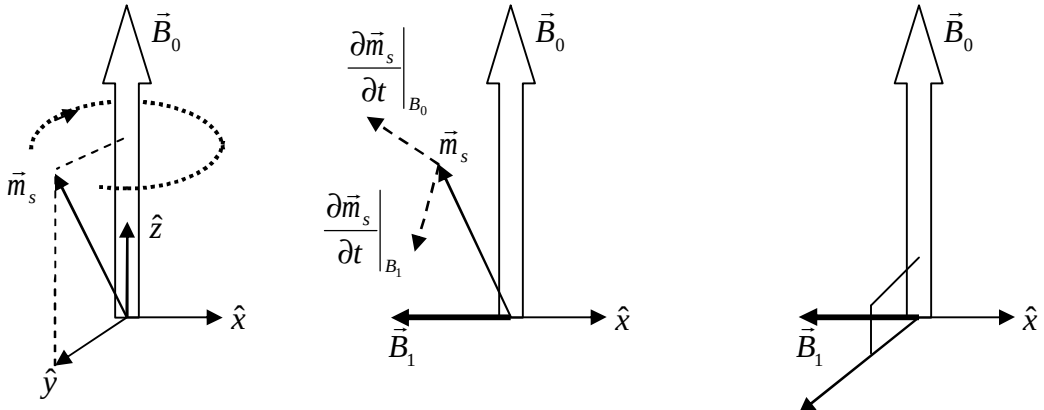

Figure II.1 NMR Sample Magnetic Moment Precession

NMR is stimulated when $\vec{m}_s$ is parallel to $\vec{B}_0$ and a $\vec{B}_1$ field, orthogonal to $\vec{B}_0$, is introduced. The $\vec{B}_1$ field is oscillated at w_0 along the $\hat{x}$ axis. The $\vec{B}_1$ field is implemented in the NMR system of Figure I.1 by surrounding the sample with a coil, whose transverse axis is along $\hat{x}$, and driving the coil with a sinusoidal voltage at w_0. Equation 2.2 is re-written to include the effect of $\vec{B}_1$ as follows,

$$\frac{\partial \vec{m}_s}{\partial t} = g\vec{m}_s \times \left[\vec{B}_0 \hat{z} + \vec{B}_1 \hat{x}\right] \tag{2.5}$$

Physically, $\vec{B}_1$ rotates $\vec{m}_s$ away from $\vec{B}_0$ as shown in Figure II.1b. $\vec{B}_1$ is oscillated synchronously to $\vec{m}_s$ where $\vec{B}_1$ always has maximum amplitude when $\vec{m}_s$ is in the y-z plane. Each time $\vec{m}_s$ is in the y-z plane, which occurs twice per cycle of $\vec{m}_s$ precession, $\vec{B}_1$ rotates $\vec{m}_s$ away from $\vec{B}_0$. The nuclear moment, $\vec{m}_s$, rotates away from the $\hat{z}$ axis at a rate $w_1 = g\left|\vec{B}_1\right|$, while precessing around $\vec{B}_0$. At time $t_{p/2} \cong \frac{p}{2w_1}$ after the $\vec{B}_1$ is introduced, $\vec{m}_s$ is orthogonal to $\vec{B}_0$. This position is critical for many NMR applications and is known as the $\pi/2$ position because $\vec{m}_s$ is $\pi/2$ radians from $\vec{B}_0$. The precession of $\vec{m}_s$ around but not parallel to $\vec{B}_0$ caused by a synchronized oscillating $\vec{B}_1$ is NMR. A sample experiences NMR when its many $\vec{m}_s$ move coherently to form the sample magnetization, $\vec{M}_s$. IDNMR and FDNMR detect the motion of $\vec{M}_s$.

b. IDNMR Detection

Inductive Detection NMR is the conventional method for exciting and detecting atoms. The IDNMR method begins after $\vec{M}_s$ is rotated orthogonal to $\vec{B}_0$, the $\pi/2$ position. The coil which creates the $\vec{B}_1$ field is disconnected from its excitation source and connected to a detection amplifier. The magnetization $\vec{M}_s$ will continue to precess in the x-y plane for many cycles and these precessions are detected by the coil. The precessing magnetic field, $\vec{B}_s$, produced by $\vec{M}_s$, passes through the coil and induces an oscillating electro-motive-force (EMF). The induced EMF appears as a sinusoidal voltage, V_0, at the coil terminals which are

connected to a high-impedance amplifier. The voltage $V_0 = \frac{-\partial\Phi}{\partial t}$, where $\Phi = \int_A \vec{B}_s \bullet \partial\vec{A}$ is the magnetic flux through the cross-sectional area, *A*, of the coil, is amplified for robust detection. This signal amplitude decays with a sample-dependent time constant as each nuclear moment in $\vec{M}_s$ interacts with its many random neighbors. Without $\vec{B}_1$, the many $\vec{m}_s$ moments lose coherent precession about $\vec{B}_0$, and $\vec{M}_s$ is reduced to zero. The nuclear moments return to the relaxed state in Figure II.1a and $\vec{M}_s$ reforms parallel to $\vec{B}_0$. The detection can resume after $\vec{M}_s$ is parallel to $\vec{B}_0$ and $\vec{B}_1$ is re-introduced to drive $\vec{M}_s$ again into the x-y plane.

c. FDNMR Detection

Force Detection NMR is a recent development in using NMR for elemental identification and analysis. FDNMR was proposed by John Sidles in 1991 [32]. The method requires coupling the rotating $\vec{M}_s$ of an excited sample to a micro-cantilever. The cantilever resonates with the motion of the $\vec{M}_s$. One can imagine a cantilever which resonates as $\vec{M}_s$ precesses around in the x-y plane. However, this precession occurs at 100MHz for hydrogen protons in a 2.35 T $\vec{B}_0$ field, and 9.8 MHz for chloride ions in the same field. Manufacturing cantilevers and detecting their motion at these frequencies is difficult. Therefore, adiabatic rapid passage (ARP) excitation is used to oscillate $\vec{M}_{s,z}$, the $\hat{z}$ component of precessing $\vec{M}_s$, at acoustic frequencies near 1 kHz, a possible resonant frequency of micro-cantilevers [24, 30]. ARP results from the frequency modulation of $\vec{B}_1$ about w_0, where

$$\vec{B}_1 = \left|\vec{B}_1\right| \cos\left[\left(w_0 + w_m \cos(w_t t)\right)t\right] \tag{2.6}$$

This excitation causes an oscillating $\hat{z}$ component of $\vec{M}_s$ at w_t, the frequency of the modulation. The frequency w_m is the modulation amplitude and w_m controls the magnitude of $\vec{M}_{s,z}$. Coherent motion of the nuclear moments in $\vec{M}_s$ is ensured by satisfying the adiabatic condition, which maintains constant sample energy and entropy excitation. To satisfy the condition, the product of w_t and w_m is limited with w_t normally

around 1 kHz [30]. By satisfying the adiabatic condition, $\vec{M}_{s,z}$ can oscillate about 200 times, driven by $\vec{B}_1$, before the nuclear moments lose coherent motion and $\vec{M}_s$ decays [35]. Differences in $\vec{B}_0$ across the sample cause the decay of $\vec{M}_s$ as the modulation of $\vec{B}_1$ can not perfectly center on the w_0 of each nuclear moment.

The oscillation of $\vec{M}_{s,z}$ at w_t from ARP must be coupled to a mechanically resonant cantilever for FDNMR. A magnet is attached to the cantilever and brought near the sample, which undergoes ARP to provide this coupling. The oscillating $\vec{M}_{s,z}$ exerts a force on the detector magnet because there is always a force, $\vec{F}_m$, between the magnetic field produced by $\vec{M}_s$, $\vec{B}_s$, and the detector magnetic moment, $\vec{M}_m$, as

$$\vec{F}_m = \nabla(\vec{M}_m \bullet \vec{B}_s) = \vec{M}_m \bullet \nabla\vec{B}_s + \nabla\vec{M}_m \bullet \vec{B}_s \tag{2.7}$$

The moment of the detector magnet, $\vec{M}_m$ (i.e., its magnetization) will experience a force when positioned in the field gradient of the sample, $\nabla\vec{B}_s$, from Equation 2.7. Any time dependency on $\nabla\vec{B}_s$ or $\vec{M}_m$ will create a time varying force. $\vec{M}_m$ is constant in time and space since it is aligned to and reinforced by the surrounding $\vec{B}_0$ field. However, $\nabla\vec{B}_{s,z}$ across the magnet is changing in time from the oscillations of $\vec{M}_{s,z}$, causing an oscillating $\hat{z}$ directed force on the magnet. The sample also experiences an oscillating force equal and opposite to that on the magnet.

Unfortunately, only a small slice of the sample experiences NMR since a field gradient is introduced into the $\vec{B}_0$ field across the sample by the small detector magnet (i.e. the sample is no longer subjected to a homogeneous $\vec{B}_0$ field) [8]. Only the sample slice where $g\,(\left|\vec{B}_0\right| + \left|\vec{B}_m\right|) = w_0$ will be excited into resonance and generate the oscillating $\vec{M}_{s,z}$; $\vec{B}_m$ is the magnetic field produced by $\vec{M}_m$. Hence, the final force between the magnet and sample is small. The Better Observation Of Magnetization, Enhanced Resolution, And No Gradient (BOOMERANG) topology of FDNMR places a second stationary magnet co-planar with and surrounding the detector magnet as illustrated in Figure II.2 [24]. This second magnet restores the $\vec{B}_0$ field

homogeneity across the sample which allows the entire sample to resonate and exert an oscillating force on the detector magnet. The BOOMERANG topology is assumed for the remainder of this analysis of FDNMR.

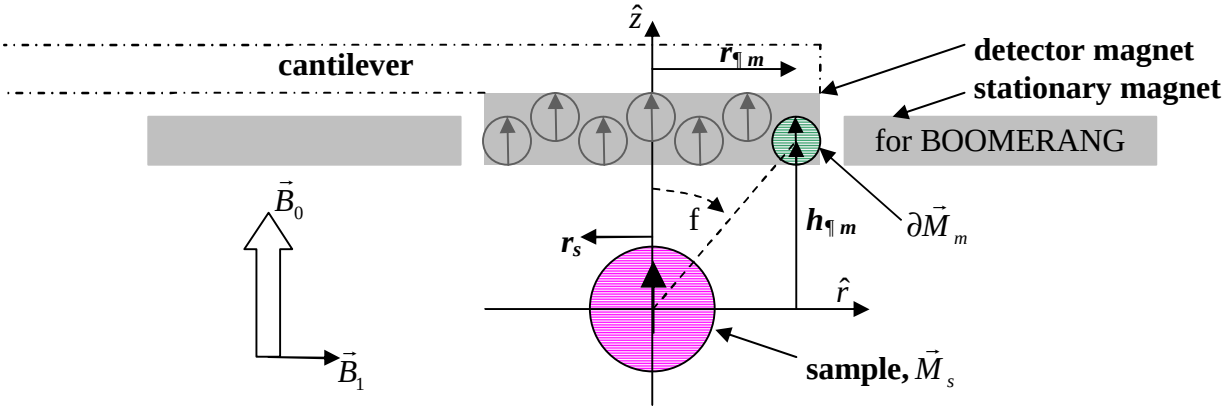

Figure II.2 Magnet-on-Cantilever FDNMR Force Schematic

Equation 2.8 quantifies the force between $\vec{M}_s$ from a uniformly magnetized spherical sample and $\partial\vec{M}_m$, a differential region of the detector magnet with vertical position, $h_{\P m}$, and lateral position $r_{\P m}$ [24].

$$\partial\vec{F}_m = \nabla(\partial\vec{M}_m \bullet \vec{B}_s) = \frac{m_0}{4p}\frac{\left|\partial\vec{M}_m\right\|\vec{M}_s\right|}{\sqrt{h_{\partial m}{}^2 + r_{\partial m}{}^2}}\left[\cos f(9-15\cos^2 f)\hat{z} + \sin f(3-15\cos^2 f)\hat{r}\right] \quad (2.8)$$

The force components are cylindrically symmetric about $\hat{z}$, canceling the $\hat{r}$ directed forces when the sample and magnet are aligned as in Figure II.2. The resulting force is solely in the $\hat{z}$ direction and magnetization of the detector and stationary magnets are assumed to remain constant. Pieces of detector magnet more than 39° off the $\hat{z}$ axis, $\phi > 39°$, experience the opposite vertical force from those closer to the $\hat{z}$ axis. This sets the optimal radius of the entire detector magnet, r_d, to 378 μm given a sample radius, r_s, of 500 μm, assuming a 100 μm gap between the sample and the magnet surface. The gap includes both a cover-slip to physically isolate the sensor from the sample and an air gap to allow unrestricted motion of the magnet.

The oscillating $\hat{z}$ axis force on the detector magnet causes it to move vertically as it is attached to a flexible cantilever. The field, $\vec{B}_1$, is driven to ensure w_t matches w_r, the mechanical resonant frequency of the underdamped cantilever. Excitation at mechanical resonance increases the cantilever motion by Q, its quality factor.

d. SNR Derivations

This section explores the quantitative SNR of IDNMR and FDNMR and presents the scaling laws with $\vec{B}_0$, r_s, and g to understand the detection of microliter samples. The detection coil for this analysis of IDNMR is a discrete component solenoid coil. Planar coils have also been considered to allow integration of the coil and detection electronics onto a micro-chip but these designs suffer from reduced signal strength, as the coil does not surround the sample [7, 33]. The planar coils exhibit more noise, since the resistance of thin film or plated interconnect is usually higher than discrete wire. Both solenoid IDNMR and FDNMR sensors can be optimized to detect a spherical sample with r_s = 500 μm (0.52 μL), as opposed to the 1 mL sample common in larger systems. The 0.52 μL sample volume is a criterion used to compare IDNMR and IDNMR in this work A 1 T $\vec{B}_0$ field is the other criterion used to compare the detection methods. The detector radius, r_d, is the common metric used to characterize each sensor.

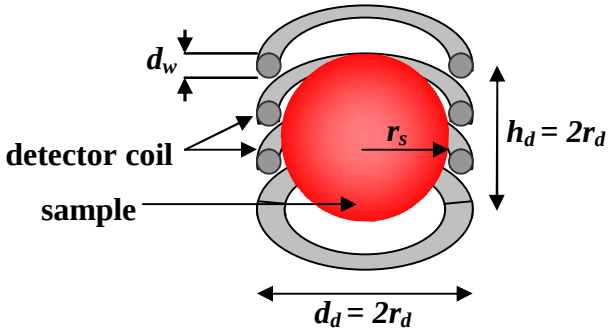

Figure II.3 IDNMR Sensor Dimensions

To determine the SNR of an IDNMR system and sample, first calculate the magnetization per unit volume of the sample, $M_{s,v}$, with Equation 2.9 from the Curie Law,

$$M_{s,v} = N \frac{g^2 \left|\vec{B}_0\right| \hbar^2 I_s (I_s + 1)}{3 k_b T} \tag{2.9}$$

N is the number of detectable atoms per unit volume of sample, I_s is the spin number of the atoms under excitation (1/2 for hydrogen protons, 3/2 for chlorine), k_b is Boltzman's constant, and T is the absolute temperature in Kelvin. Equation 2.10 specifies the coil sensitivity, B_1 / I. The coil sensitivity is the magnetic field induced in the coil by a unit of current,

$$B_1 / I = \frac{m_0 h_d}{k_p d_w d_d \sqrt{1 + (h_d / d_d)^2}} \tag{2.10}$$

m_0 is the permeability of free space, h_d is the height of the detector coil , k_p is the ratio between wire pitch and wire diameter of the coil, d_w is the diameter of the coil wire, and d_d is the diameter of the detector coil. Equation 2.11 defines the resistance of the detector coil,

$$R_c = \frac{4 r h_d d_d}{k_p d_w^3} \tag{2.11}$$

r is the resistivity of the coil wire material, $2.65 * 10^{-8}$ Ω-m for aluminum. High-frequency effects on R_c are ignored as the skin depth of aluminum wire is 5.5 μm when w_0 = 100 MHz (2.35 T system and hydrogen sample) and rises to 11.1μm at 25 MHz (0.6 T system). Both of these depths are comparable to or greater than half the 12.7 μm diameter of 56 gauge wire used in the coil. Equation 2.12 quantifies the EMF induced voltage across the coil terminals by a sample at resonance in the π/2 position [21],

$$EMF\ Voltage = w_0 (B_1 / I) V_s M_{s,v} \tag{2.12}$$

for a spherical sample of volume, $V_s = (4/3)\pi r_s^3$. Thermal vibrations in the coil wire atoms cause Johnson noise in the coil current. The current noise generates a noise voltage as

$$Thermal\ Noise\ Voltage = \sqrt{4 k_b T R_c \Delta f} \tag{2.12}$$

Δf is the bandwidth of detection system. The complete SNR of IDNMR is

$$SNR_{IDNMR} = \frac{EMF\ Voltage}{Thermal\ Noise\ Voltage} = \frac{w_0 (B_1 / I) V_s M_{s,v}}{\sqrt{4 k_b T R_c \Delta f}} \propto \frac{g^3 \left|\vec{B}_0\right|^2 r_s^3}{r_d}, \tag{2.13}$$

where simplifying assumptions are made that $h_d = d_d = 2r_d$ as in Figure II.3 [21]. Equation 2.13 considers the voltages in the coil, not the circuit noise of amplifiers or deviations from the assumption of a constant $\vec{M}_m$. The last term in Equation 2.13 allows a comparison of sample materials, magnetic field strengths, sample sizes, and detector sizes.

The forces of FDNMR predict a SNR as the ratio between the magnetic force between the sample and detector magnet and the noise force from damping of the detector magnet.

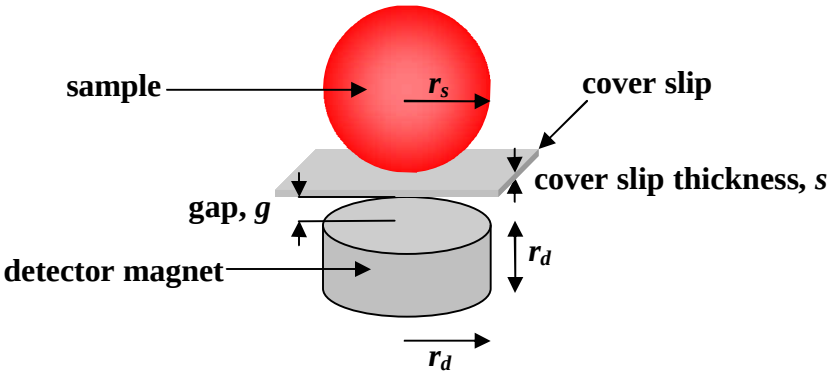

Figure II.4 FDNMR System Dimensions

The total force between the sample and detector magnet given by the integral of Equation 2.8, resulting in

$$\vec{F}_m = Magnetic\ Force = \int_{V_m} \nabla(\partial \vec{M}_m \bullet \vec{B}_s) = m_0 K_f \left|\vec{M}_m\right| M_{s,v} V_s \tag{2.14}$$

V_m is the volume of the detector magnet and K_f is a shape factor resulting from the closed for integral in Equation 2.14. K_f accounts for the geometry of the system, as

$$K_f = \frac{r_d^{\,2}}{2}\left[\frac{1}{(r_d^{\,2}+r_t^{\,2})^{3/2}} - \frac{1}{(r_d^{\,2}+(r_t+r_d)^2)^{3/2}}\right] \tag{2.15}$$

r_t is the total distance between the sample center and the near face of the detector magnet ($r_t = r_s + s + g$). The detector magnet disc has equal thickness and radius in this model to constrain the number of design paramenters. The damping noise force on the magnet in Equation 2.16 results from viscous air flow and two Brownian noise sources, molecular impingement and structural dissipation. Magnetic damping from eddy currents in the stationary magnet is assumed to be insignificant.

$$Damping\ Noise\ Force = \sqrt{4k_b T D \Delta f} \tag{2.16}$$

Equation 2.17 defines the damping factor, D, where the first bracketed term determines squeeze film damping from viscous air flow between the disk magnet and the cover slip. This dominates in the regime where the gap is smaller than the mean free path of ambient air molecules ($g < l_{mfp}$) [27]. The second term applies to the regime where $g > l_{mfp}$ and quantifies the dissipation from molecules impinging on the magnet due to their Brownian motion.

$$D = \frac{n_0 r_d^{\,4}}{g^3}\left[\frac{1.5pP_{torr}}{760} + \frac{1}{1+9.6K_n^{\,1.16}}\right] = \frac{m_{eff} w_t}{Q} \tag{2.17}$$

n_0 is the viscosity of air, P_{torr} is the air pressure in Torr surrounding the magnet, K_n is the Knuden number of the system ($\frac{5x10^{-5}}{P_{torr}\,g}$), and m_{eff} is the effective mass of the cantilever assembly. The silicon cantilever in this work is single-crystal-silicon and has an inherent quality factor, Q, which can approach 100,000 from structural dissipation in the absence of molecular impingement. The ratio between magnetic force and damping noise force in Equation 2.18 determines the SNR of FDNMR, with the reduced expression allowing performance comparisons between the sensor design parameters.

$$SNR_{FDNMR} = \frac{Magnetic\ Force}{Damping\ Noise\ Force} = \frac{m_0 K_f \left|\vec{M}_m\right| M_{s,v} V_s}{\sqrt{4k_b TD\Delta f}} \propto g^2 \left|\vec{B}_0\right| r_s^3 \left[\frac{1}{(r_d^2 + r_t^2)^{3/2}} - \frac{1}{(r_d^2 + (r_t + r_d)^2)^{3/2}}\right] \tag{2.18}$$

e. SNR Comparison

To compare the two NMR methods, we consider the sample and detector radii to be equal to r, the system radius. SNR_{IDNMR} decreases faster than SNR_{FDNMR} when either g, $\left|\vec{B}_0\right|$, or r are reduced because SNR_{IDNMR} has a greater dependency on each than SNR_{FDNMR}. The quantitative dependencies are summarized in Table II-1.

Table II-1 Exponential Dependencies of NMR SNR

	g	$\left\|\vec{B}_0\right\|$	r
IDNMR	3	2	2
FDNMR	2	1	~ 1

Figure II.5 presents quantitative comparisons of the SNR for detecting the hydrogen atoms of water and chloride ions in a 1 wt% aqueous solution. The magnetic field, $\vec{B}_0$, and the system radius, r, are scaled down, and Δf is 1 Hz. The time necessary achieve a 1 Hz measurement bandwidth is dependent on the filtering and speed of equipment used to capture the sensor output. For IDNMR, the coil wires are 56 gauge (12.7 μm diameter) aluminum on a 25 μm pitch (k_p =2), and r_s is 30 μm smaller than r_d to allow space for a separation tube wall not shown in Figure II.3. In the FDNMR cases, s is 50μm, g is 50 μm. The equivalent Q

from squeeze film damping is 430 at 760 Torr and 10,000 at 2.5 mTorr. The pressure drop increases SNR_{FDNMR} by a factor of 4.8.

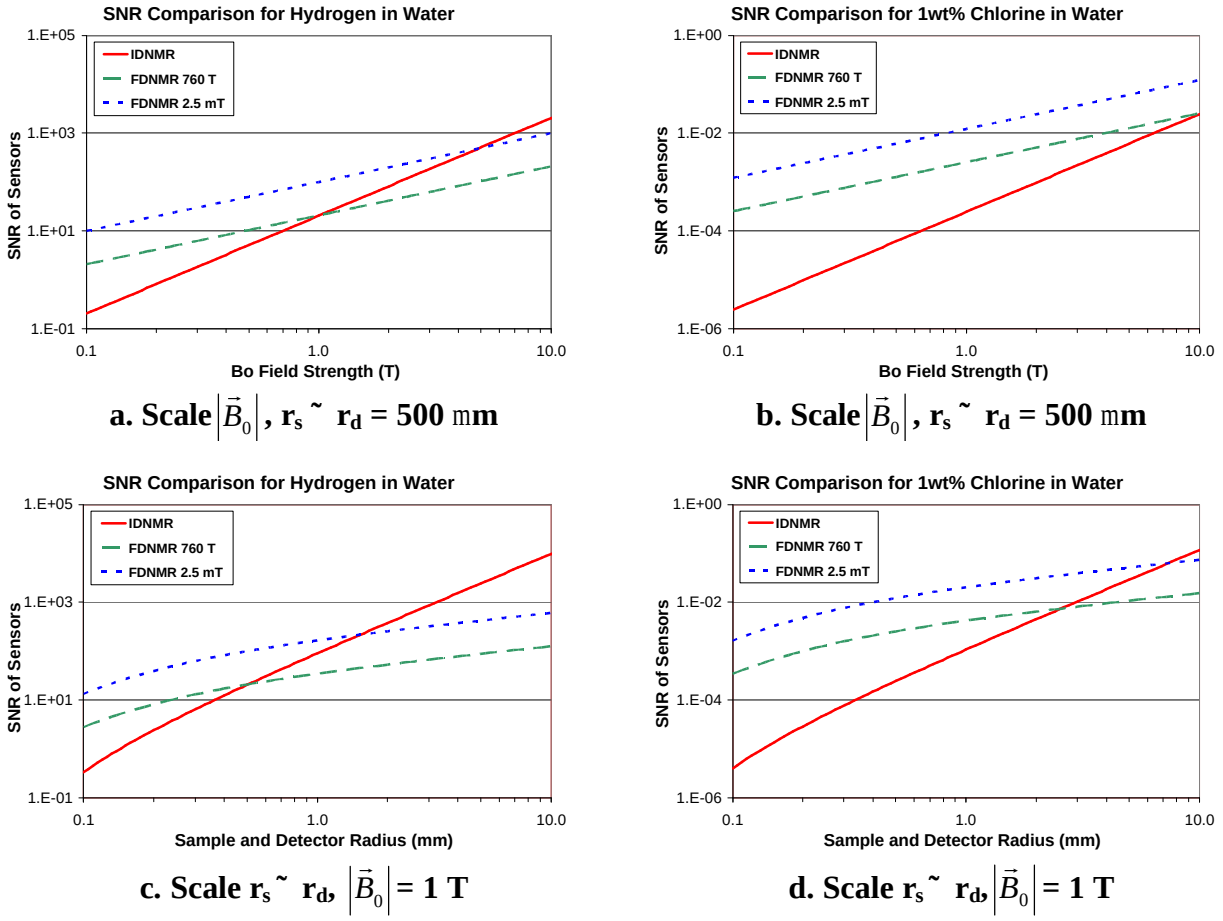

a. Scale $|\vec{B}_0|$, r_s ~ r_d = 500 mm

b. Scale $|\vec{B}_0|$, r_s ~ r_d = 500 mm

c. Scale r_s ~ r_d, $|\vec{B}_0|$ = 1 T

d. Scale r_s ~ r_d, $|\vec{B}_0|$ = 1 T

Figure II.5 Quantitative SNR Comparisons

SNR_{IDNMR} always drops below SNR_{FDNMR} at a crossover point as the scaling factor decreases in the plots of Figure II.5. The scaling factor values at crossover are highlighted in Table II.2. As summarized in Table II-3, both systems have the same SNR of 21 at 760 Torr with the 0.52 µL V_s and 1 T $\vec{B}_0$ field criterion. SNR_{FDNMR} increases to 100 at 2.5 mTorr. Considering the comparison criteria, the SNR_{FDNMR} of a 1 wt% aqueous chloride solution, 0.0025, is 8100x smaller than the hydrogen in water because $g_{Cl} \cong 0.1\ g_H$, $N_{Cl} \cong 0.0025\ N_H$, and $I_{s,Cl} = 3\ I_{s,H}$. The SNR_{IDNMR} of the chlorine solution is 84000x smaller than the hydrogen case because of the additional dependency on g. The absolute SNR values indicate that FDNMR is comparable or better than IDNMR at detecting microliter hydrogen samples in low $\vec{B}_0$ field strengths. Detecting chlorine

requires both a stronger solution of chlorine and a further reduction in measurement bandwidth to reach an SNR of 1.

Table II-2 SNR Crossover Points

	Hydrogen	**Chlorine**
Scale $\left\|\vec{B}_0\right\|$, 760 T	1.0 T	10 T
Scale $\left\|\vec{B}_0\right\|$, 2.5 mT	4.8 T	48 T
Scale r_d, 760 T	510 μm	2.5 mm
Scale r_d, 2.5 mT	1.5 mm	7.3 mm

Table II-3 Criterion System Comparison

	Hydrogen	**Chlorine**
SNR_{IDNMR}	21	$2.5*10^{-4}$
SNR_{FDNMR}, 760 T	21	$2.6*10^{-3}$
SNR_{FDNMR}, 2.5 mT	100	$1.2*10^{-2}$
IDNMR Voltage	68 nV	0.81 pV
FDNMR Force	1.0 pN	120 aN

The absolute voltage and force generated by IDNMR and FDNMR are presented in Table II-3. Detecting the 1.0 pN FDNMR magnetic force from a hydrogen sample is the goal for the FDNMR sensor in this work.

III. FDNMR Sensor Design

The previous section on NMR physics and SNR clearly indicates that FDNMR is a technology capable of detecting NMR in microliter samples. However, detecting the FDNMR signal for hydrogen samples requires sensing a single piconewton of oscillating force on the magnet normal to its face. The primary goal of the FDNMR sensor chip is to translate this tiny force to a resonant cantilever motion approaching 1 nm. This motion can then be converted to a voltage by a capacitive bridge and amplification electronics. This chapter first presents the overall sensor technology, fabrication, and materials. Second, the mechanical cantilever is designed to achieve desired resonant characteristics. The third section describes the integrated capacitors which surround the cantilever for actuation and sensing. A self-test actuator can displace the cantilever and the capacitive bridge is simulated to model the conversion between cantilever displacement and voltage. Fourth, the electronics used to amplify the capacitive bridge output signal for external measurement are described.

a. Fabrication Technology and Materials

The cantilever transducer for the FDNMR sensor is made using modern fabrication technology for integrated circuit (IC) manufacturing. The IC processing provides two critical contributions to creating the full sensor on a single chip. First, the capacitive bridge can have dimensions in microns, allowing detection of nanometer and smaller displacements. Second, the IC technology allows on-chip electronic amplification of the small, high-impedance electrical signals generated by the capacitive bridge. After this occurs, the signals can be transmitted over long wires to external equipment without significant degradation of the signal quality. Without the on-chip amplification, the load capacitance from the wires would reduce the sensitivity of the capacitive bridge to cantilever displacement.

The fabrication of the FDNMR chip begins with the 3-metal foundry CMOS process from Austria Microsystems (AMS) on a 535 μm thick, 150 mm diameter single-crystal silicon wafer [2]. The AMS process allows 0.6 μm minimum transistor lengths and 1 μm aluminum interconnect widths. Many user designs are fabricated on the wafer simultaneously to share the time and cost of the processing. Each complete multi-user wafer has 28 reticles of 36 chips arrayed across its surface. Each reticle measures 2 cm by 2 cm and is partitioned into 36 different chip designs, contributed by various customers. One of these

designs is the FDNMR chip. Therefore, 28 replicates of the FDNMR chips are fabricated on a wafer, one per reticle. The individual chips are diced apart, grouped by design, and returned to the multiple users. The FDNMR chips measure 2.5 mm on a side with surface features outlined in Figure III.1. There are 10 wafers in the engineering run of the CMOS process, of which one was diced for this work. The original chips from the AMS foundry are not micromachined, so the cantilevers are immobile and further processing is necessary to enable the sensitive displacement sensor.

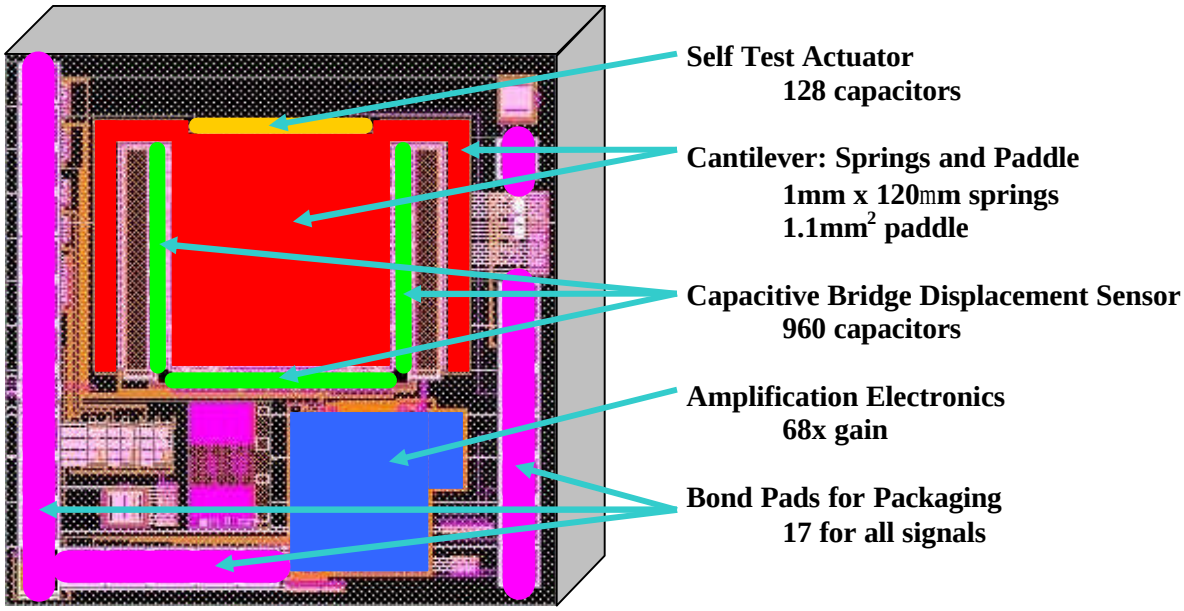

Figure III.1 FDNMR Sensor Floorplan

The process of removing select regions of material to create a mechanically active CMOS-MEMS device from the chip fabricated by AMS is performed entirely at Carnegie Mellon [16, 36, 39]. The FDNMR method stipulates that the cantilever, comprised of two spring beams and a paddle, should resonate around 1 kHz. However, it is difficult to etch a sufficiently thin cantilever, so 5 kHz is chosen as the design criterion in this work. The silicon wafer and hence the silicon base of the chip is 535 μm thick, but this must be thinned to a 50μm thick membrane to enable vertical resonance at 5 kHz with reasonable (1 mm) length cantilever spring beams. Reducing the thickness to 18μm will enable a 1 kHz cantilever. A 5 kHz cantilever requires removing 485 μm of silicon from the backside of the chip, beneath the cantilever and the capacitive bridge. Furthermore, the membrane must have an evenly etched surface to ensure uniform thickness along the two spring beams and across the paddle. A non-uniform thickness leads to unequal curling and irregular resonant

modes. Finally, the cavity size and location must be constrained to the region of the cantilever and capacitive bridge, as bond pads are 150 µm from the open region around the cantilever. The bond pads must be supported by thick anchored silicon to endure the stress of the wire-bonding process. The fabrication sequence is shown in Figure III.2. Figure III.2a is the cross-section of the chip direct from the foundry. The chip backside is patterned and etched to a depth of 485 µm in Figure III.2b, using photolithography and the Bosch deep-reactive-ion-etch (DRIE) process [22]. The backside pattern is aligned using the edges of the chip as guides. Next, the detection magnet is attached to the etched backside cavity surface with glue, see Figure III.2c.

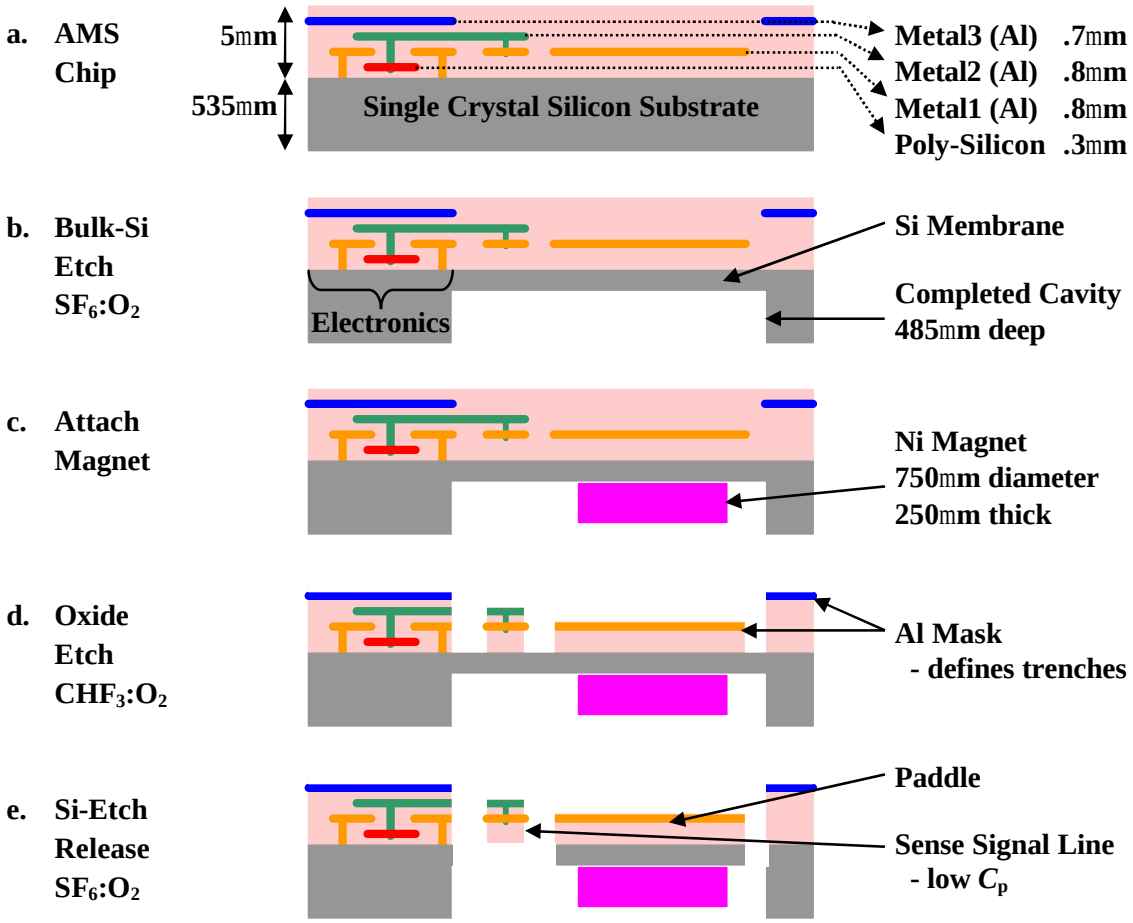

Figure III.2 FDNMR CMOS-MEMS Fabrication Sequence

Two steps are necessary to etch and release the paddle, its suspension spring beams, and the capacitive bridge. The CMOS process photolithographically defines patterned metal layers to form the cantilever geometry. Additional metal line patterns form the individual capacitors of the capacitive bridge and interconnect wiring with short metal lines periodically tethering the capacitors and interconnect to the

chip. In CMOS-MEMS, the aluminum interconnect of the CMOS process defines the patterns. Aluminum is ion milled slowly in subsequent reactive-ion etch steps, and thus acts as a mask for silicon dioxide (SiO_2), the dielectric material between metal layers, and for silicon. In the first etch and release step, a CHF_3:O_2 plasma anisotropically etches the exposed SiO_2 in Figure III.2d. The DRIE Bosch process is then used as the second step to etch through the remaining 50 μm silicon layer in Figure III.2e, and the chip is released. The released cantilever assembly comprises a 4 μm thick CMOS interconnect layer stack and an underlying 50 μm thick single-crystal silicon layer. Because there is approximately 2 μm of lateral undercut of silicon during the silicon release etch in Figure III.2e, structures laid out less than 4 μm in width will be completely undercut with no silicon present underneath. This kind of structure is used to make the interconnect from the capacitive bridge to the amplification electronics with little parasitic capacitance to substrate, C_p.

Successful completion of the etching process defined above is the principle challenge of the FDNMR chip fabrication. The detailed fabrication approach and results are presented in the experimental section of this thesis. Research groups have developed several other methods to etch silicon and fabricate cantilevers and suspended silicon devices. However, creating a large 10 μm to 50 μm thick membrane etched from a CMOS chip with constrained area and position, near-vertical sidewalls between membrane and chip, a flat etched and exposed surface, and separating the membrane into a cantilever and additional structures is unique to this work. Wet silicon etchants, such as tetra-methyl-ammonium-hydroxide (TMAH) and potassium-hydroxide (KOH), can etch a {110} crystalline silicon surface and maintain a flat bottom {100} surface to create the membrane, but the walls slope outwards at 54.7° on {111} planes. The slope can be compensated but these chemicals are also very aggressive and few materials are an effective mask to the etchants. Thermally grown silicon oxide can not be grown on the CMOS chips without destroying the aluminum and electronic components. Epoxy-based mask materials are difficult to remove from the chip to allow further processing [25]. Many varieties of dry etching also create cantilevers. The SCREAM process can manufacture beams 20 μm thick, but only up to 5 μm wide as the process relies upon an isotropic release step to undercut structures [31]. This process also does not leave the backside accessible for magnet attachment. An alternative process, HARPSS, allows polysilicon to be considered as the cantilever material but beams are

still limited to widths of single microns [3]. A SF_6:O_2 RIE has been characterized to etch 7mm by 7mm areas across a wafer but only the center etch depth versus position on wafer was studied [1]. Prior work on DRIE has demonstrated 300 μm and deeper etches of isolated trenches, but is limited to widths of 20 μm [4]. Similar work has also investigated the interface between the sidewall and bottom surface of up to 100 μm wide trenches, but only in the region within several microns of the juncture [10]. The sidewall angle of 2.1 mm wide, 300 μm deep DRIE cavities was modeled and tested, however the etched surface uniformity was not an optimized parameter [14].

The detection magnet attached in Figure III.2c is a disc of 99.99% pure nickel foil for five reasons. First, nickel is not a permanent magnet, so its presence will not affect the plasma processing to fabricate the chip. Second, the nickel will not be strongly attracted to ambient soft magnetic materials which could damage the assembled sensor. Third, pure nickel has a well-known magnetization of 0.6115 T when placed in a stronger field and is a frequent calibration material. The known magnetization allows reliable calculations of the FDNMR force exerted on it. The $\vec{B}_0$ field strength is assumed sufficient to overcome the self-demagnetization of the detector magnet because of its low 1:2 aspect ratio. Fourth, nickel is simple to machine to a desired size since it is not brittle. Fifth, nickel is chemically stable, so it will not oxidize or change properties in the oxygen-rich environments of processing and final use.

b. Micro-Cantilever Assembly

The cantilever is composed both of single-crystal silicon and CMOS interconnect layers. Since these materials are grown or deposited at different temperatures, they have internal stress levels and the composite structure has a stress gradient. Many CMOS-MEMS structures curl vertically from the stress gradient. The thick silicon layer minimizes this effect by dominating the cantilever thickness [36]. The silicon layer and cantilever design ensure that after release, the paddle edges are aligned to the chip surface to within ±2μm. The small misalignment permits linear displacement to voltage transduction from the capacitive bridge [37].

a. Cantilever with an end plate mass **b. Cantilever with a folded plate mass**

Figure III.3 Cantilever Spring Topologies with Applied Force

Many cantilevers are long beams with a mass attached to the end, as shown in Figure III.3a. To achieve a 5 kHz resonance, the cantilevered structure is 1.2mm long. Unfortunately, in the design, the mass (shown in grey) will rotate upon applied force, which compromises the FDNMR operation. Such a long structure will also curl more at its non-anchored end causing misalignment in the capacitive bridge surrounding the mass. To resolve these problems, the FDNMR chip has the folded plate mass topology in Figure III.3b. The mass folds back along the spring beams so the end near the anchors will align to the chip surface again. This topology makes the resonant frequency design specification more challenging because of a factor of four increase in spring constant for an equal length suspension, but it promotes uniform mass displacement under an applied force. The fabricated cantilever solid model is shown in Figure III.4a. The mass is a large paddle with an attached magnet. The suspension is made from two spring beams along the chip surface which connect to the paddle by short truss beams. The topology ensures motion keeping the paddle parallel to the chip surface, which increases the capacitive bridge sensitivity to displacement.

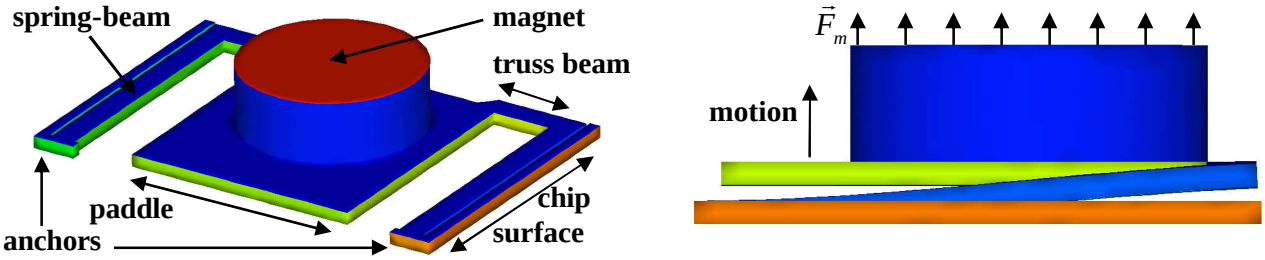

a. Cantilever with magnet, at rest **b. Cantilever with magnet, displaced**

Figure III.4 Cantilever Assembly Structure and FEM Simulated motion of Cantilever

Vertical paddle motion is made to be the first resonant mode by increasing the width of the spring beams relative to their thickness. The resonant mode can be calculated from the distributed mass of the spring beams and paddle and from the spring constant. If the complete suspension is considered to be two guided-end beams the spring constant, *k*, is given by

$$k = 2Ew\frac{t^3}{l^3} \tag{3.1}$$

E is the Young's modulus, *w* is the width, *t* is the thickness (dimension in the direction of motion), and *l* is the length. For the FDNMR sensor, the spring beams are designed 120 μm wide to allow 10 μm of over-etching

on either side during processing. The resulting 100 μm width, which is twice the silicon beam thickness, separates the first vertical and lateral resonant frequencies by a factor of 2.

Figure III.4b displays the displacement of the cantilever under a distributed magnetic force, as predicted by a finite-element-model (FEM) in Coventorware [13]. Placing a 750 μm diameter detector magnet with an edge 50 μm from the paddle edge near the truss beams results in parallel motion for any cantilever thickness near 50 μm.

The cantilever must vertically resonate at or below 5 kHz, and that frequency, w_r, is defined as

$$w_r = \sqrt{\frac{k_z}{m_{eff}}} \tag{3.2}$$

k_z is the vertical string constant, with similar dependencies to Equation 3.1, and m_{eff} is the effective mass of the cantilever and is linear with magnet and cantilever thickness. Cantilever thickness and length have the strongest impact on the vertical resonant frequency. The length is set at 1 mm to match the $1mm^2$ paddle size. A fixed 750 μm diameter magnet and a 500 μm radius sample are assumed in design. The silicon thickness can be set arbitrarily by the cavity etching sequence during fabrication. Nickel of many thicknesses is also available to be the detector magnet and change the effective mass.

The design space includes silicon thicknesses from 20 μm to 80 μm, and the nickel magnets from 200 μm to 500 μm thick. The combined CMOS layers on the structure are neglected as they are only 1.7 μm thick with a Young's modulus of 70 GPa, compared to 165 GPa for single-crystal silicon. Finite-element modeling in Coventorware is used to determine exact spring constants beyond the simple guided-end beam formula of Equation 3.1 [13]. The k_z values are compared to the analytic model for a crab-leg spring with perfect anchors in Figure III.5 [15]. The finite-element model indicates the chip surface and paddle bend slightly at their connection to the spring beams in the mode shape extracted from Figure III.4b. The perfect anchor analytic model is scaled down by 1.85 to match the soft anchor condition indicated by the finite-element results to form the solid red line in Figure III.5. This creates the final k_z model for a fixed beam width of 120 μm and beam thickness, t_{Si}, in microns where $k_z = 0.0101t_{Si}^3 + 0.2364t_{Si}^2 - 3.8099t_{Si}$.

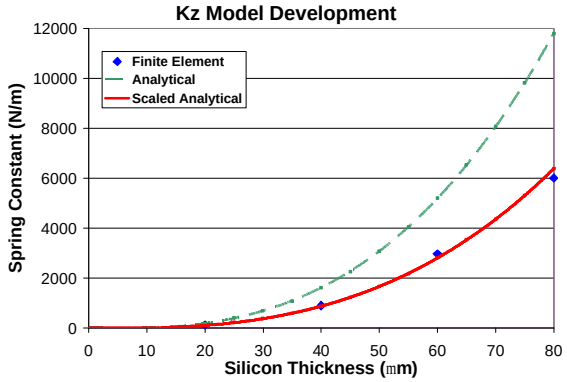

Figure III.5 Resonant Cantilever Model Development

The total effective mass, m_{eff}, in Equation 3.3 is the sum of the spring mass, $m_{sm}t_{Si}$ (weighted by $a_{eff,sm}$), the mass of the silicon paddle, $m_{pdl}t_{Si}$, and the mass of the magnet, $m_{mag}t_{Ni}$.

$$m_{eff} = (a_{eff,sm}m_{sm} + m_{pdl})t_{Si} + m_{mag}t_{Ni} \tag{3.3}$$

t_{Ni} is the thickness of nickel in microns. The mode shape of the spring beams and truss beams is used to calculate the effective mass coefficient, $a_{eff,sm}$, from Equation 3.4 where $d(x)$ is the vertical displacement along the spring length and l is the length of the beam.

$$a_{eff,sm} = \frac{1}{l * d(l)_{\max}^{2}} \int_{0}^{l} d(x)^2 dx \tag{3.4}$$

The final model for m_{eff} is $(0.4\times7.69\times10^{-10} + 2.57\times10^{-9})t_{Si} + 3.94\times10^{-9}t_{Ni}$.

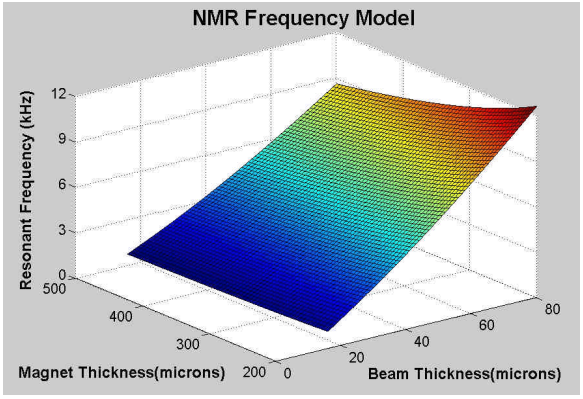

a.

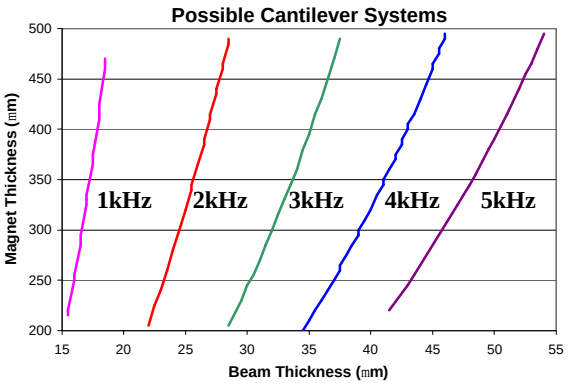

b.

Figure III.6 Resonant Cantilever Model and Design Options

The design space, as plotted in Figure III.6a, includes systems which resonate from 1 kHz to 13 kHz. Figure III.6b also identifies specific combinations of silicon cantilever and nickel magnet thicknesses that

resonate at 1, 2, 3, 4, and 5 kHz. An 18 μm thick cantilever with a 400 μm thick magnet will resonate at 1 kHz. This work aims to complete a sensor with a 50μm thick silicon cantilever and 250μm thick nickel magnet, which resonates at 6.1 kHz. This design can demonstrate complete sensor functionality before attempting the more challenging fabrication necessary to achieve the 1 kHz w_r preferred for FDNMR.

The 50 μm t_{Si} cantilever is constructed of primarily single-crystal silicon, which should reach a quality factor, Q, of at least 10,000 in vacuum. At resonance, the displacement amplitude is

$$d_z = \frac{\left|\vec{F}_m\right| Q}{k_z} \tag{3.5}$$

where $\left|\vec{F}_m\right|$ is a result of Equation 2.14. With a 250 μm t_{Ni} magnet, and assuming Q = 10,000, a 1 pN FDNMR force causes the sensor to move vertically 0.1 Å at resonance. The noise floor of the capacitive bridge is around 0.5 Å [37]. The same operating conditions with an 18 μm t_{Si} cantilever will move 1.5 Å, which is within expected measurement capabilities of the capacitive bridge. However, the silicon thickness of such a thin cantilever will not dominate the thermal stress in the CMOS interconnect to keep the cantilever flat. All edges of the capacitive bridge are designed to curl together when no magnet is attached to the paddle. However, the rigid magnet will disturb the curl-matching as it prevent the paddle from curling opposite the spring beams. This may violate the ±2 μm vertical misalignment tolerance of the capacitive bridge.

c. Electromechanical Self-Test Actuator and Capacitive Bridge

Interdigitated-finger sidewall capacitors completely line all four edges of the paddle on the FDNMR chip to both induce and measure vertical displacement of the cantilever. A simplified view of Figure III.1 is shown in Figure III.7 to highlight the finger locations, layout, and support structure. A set of 129 fingers line the edge of the paddle near the truss beams; 64 are connected to the paddle and 65 are connected to the chip surface. These fingers are self-test fingers and the 128 lateral gaps between the interdigitated fingers form an electrostatic self-test actuator. 504 fingers line the remaining three sides of the paddle. Each of the 480 lateral gaps between these fingers are electrically split into two individual capacitors. The 960 individual capacitors are connected in a bridge configuration to measure cantilever displacement. All the self-test and bridge fingers are made from three stacked layers of aluminum, with SiO_2 between the layers. Figure III.1

highlights the finger locations, layout, and support structure from Figure III.1

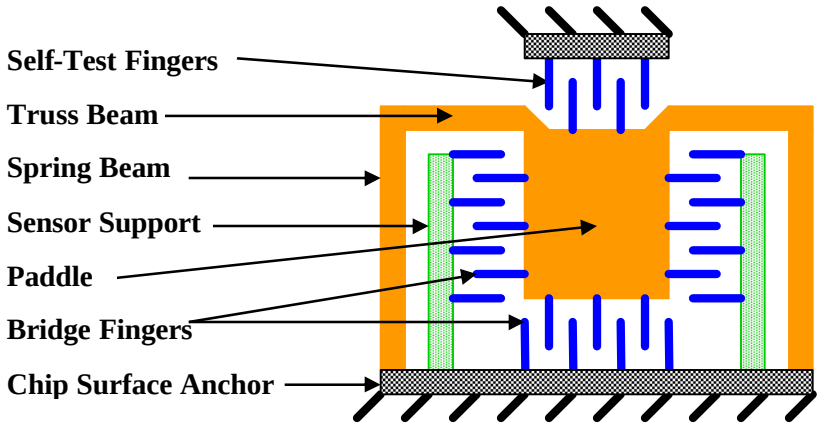

Figure III.7 Core Sensor Component Locations

Figure III.8a is a 3-dimensional model of a five finger, four gap configuration common to both self-test and sense fingers. Each lateral gap between fingers is 2 µm wide and 25 µm long. The lateral gap capacitor design is modeled using the finite-element modeling software, FemLAB, to predict capacitance when voltage is applied and one set of fingers is vertically offset from the other [12].

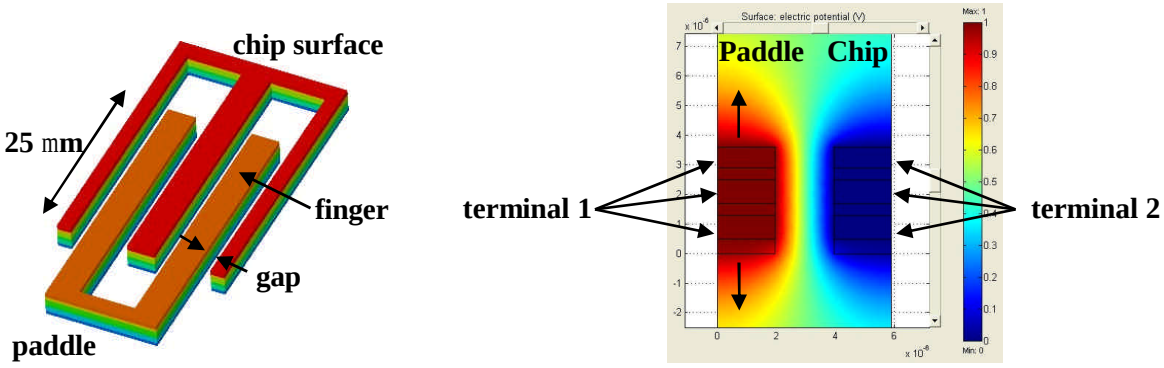

a. 3-D Finger Model **b. FemLAB Self-Test Gap Model**

Figure III.8 Self-Test Actuator Models

In the self-test actuator, all three layers of aluminum in each finger are connected together to form two electrical terminals. Terminal 1 is the paddle finger aluminum and terminal 2 is the chip surface finger aluminum in Figure III.8b. FemLAB calculates the total charge on the aluminum layers of terminal 1 when one volt is applied between the terminals; this is the capacitance between the two terminals (C = Q/(1V)). The total capacitance of all 128 gaps vs. vertical finger offset is plotted in Figure III.9a. The self-test actuator is designed to deflect the paddle vertically if the fingers are offset. When a voltage is applied between the

terminals, the terminals experience an electrostatic force in the direction that increases the capacitance between them. Equation 3.6 gives the electrostatic force. The fingers are constrained to vertical motion by the folded cantilever suspension. Therefore, the electrostatic force will pull the paddle vertically towards zero micron offset since that position has the highest capacitance.

$$F = \frac{1}{2}\frac{\partial C}{\partial z}V_{dc}^{\ 2} \tag{3.6}$$

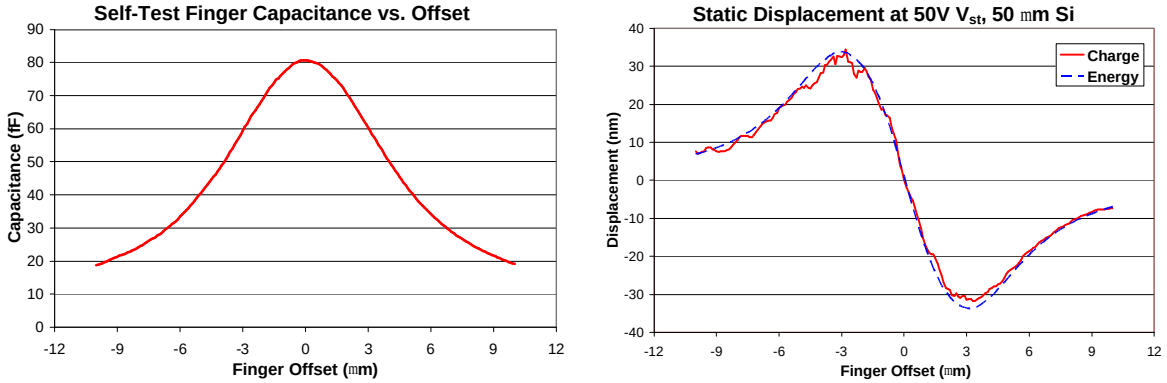

a. Total Self-Test Capacitance **b. Electrostatic Cantilever Displacement**

Figure III.9 Self-Test Capacitance and Displacement

Figure III.9b displays the expected cantilever displacement when a constant 50 V is applied to a self-test actuator with initial offsets from -10 µm to +10 µm. A 50 µm thick cantilever will move a maximum 34 nm under the applied electrostatic force. The jagged "Charge" line uses the charge model for calculating capacitance. The smoother and dashed blue "Energy" line represents another method of determining the capacitance where FemLAB tabulates the total energy of the system in Figure III.8b.

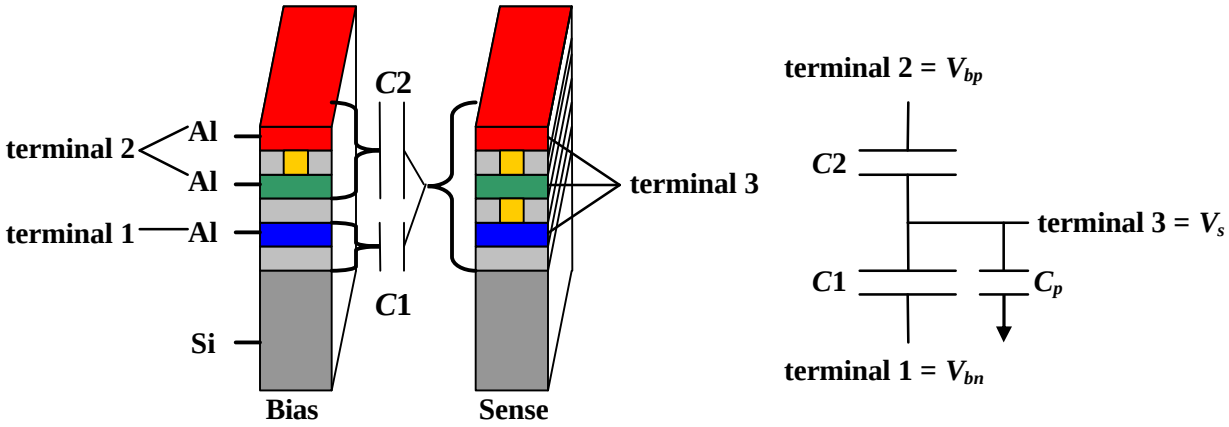

a. Bridge Finger Detailed Capacitor Structure **b. Capacitive Divider Schematic**

Figure III.10 Bridge Finger Design

The sense fingers of the capacitive bridge share the same geometry in Figure III.8 as the self-test fingers but the electrical connections and functions of the aluminum layers are different. One finger applies bias voltages across the gap, while the other finger senses an induced voltage. In the detail of Figure III.10a, the bias finger metal layers are split into two terminals; the bottom metal layer is terminal 1 and the top two metal layers are connected as terminal 2. All three metal layers of the sense finger are connected together at terminal 3. The gap between terminals 1 and 3 forms capacitor $C1$, while the gap between terminals 2 and 3 forms capacitor $C2$. Figure III.10b is the electrical schematic of the capacitive divider formed by the terminals and gap between the bias and sense fingers. There is a parasitic capacitance, C_p, from terminal 3 to ground. To operate the divider, bias voltages, V_{bn} and V_{bp} are applied respectively to terminals 1 and 2 of the capacitive divider, respectively. The divider sense voltage on terminal 3, V_s, is a function of $C1$ and $C2$ as,

`

$$V_s = V_b \frac{C2 - C1}{C2 + C1 + C_p} \tag{3.7}$$

V_{bp} and V_{bn} have opposite polarity and equal amplitude, V_b, where $V_{bp} \geq 0$ and $V_{bn} \leq 0$. Any displacement of the cantilever will change the ratio between $C1$ and $C2$ and cause a corresponding change in the V_s, generating transduction from displacement to voltage. Figure III.11a is a representative FemLAB simulation used to calculate $C1$ and $C2$ across one gap as a function of vertical offset, where 1 volt is applied to terminal 2. $C1$ and $C2$ from 120 gaps are plotted in Figure III.11b, where the bias finger moves vertically and C_{eq} is the sum of $C2$ and $C1$ when they both decrease as the finger offset increases above zero microns.

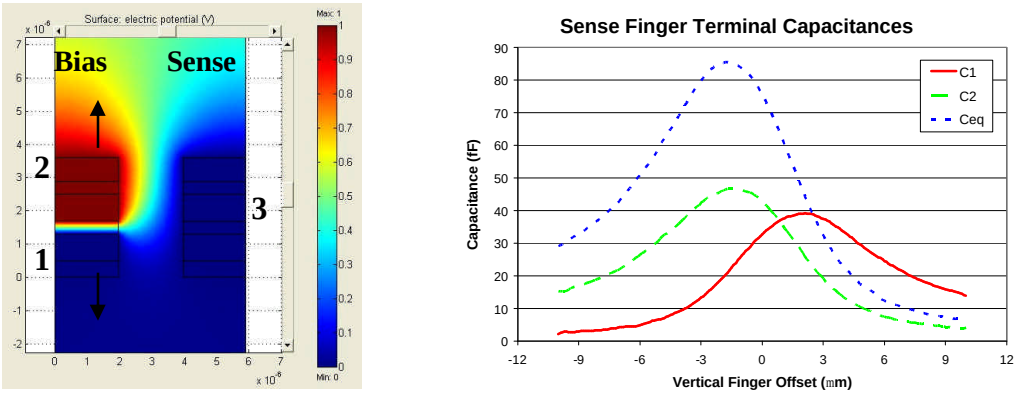

a. FemLAB Sense Gap Model **b. Total Sense Capacitances**

Figure III.11 Capacitive Divider Models

The 504 bridge fingers are separated into 24 units with four different electrical and mechanical arrangements, A, B, C, and D, as shown in Figure III.12a. Each arrangement has two terminal voltages, a sense voltage, and a mobile finger. The four arrangements define sense capacitors to create the balanced capacitive bridge shown in Figure III.12b. $C1_A$, $C1_D$, $C2_B$, and $C2_C$ decrease while $C1_B$, $C1_C$, $C2_A$, and $C2_D$ increase if the mobile fingers rise as shown by the arrows in Figure III.12a. Increasing and decreasing pairs of $C1$ and $C2$ are wired in parallel to form balanced capacitive dividers. This makes the sense voltages, V_s and V_s', equal zero volts when the vertical offset equals zero microns.

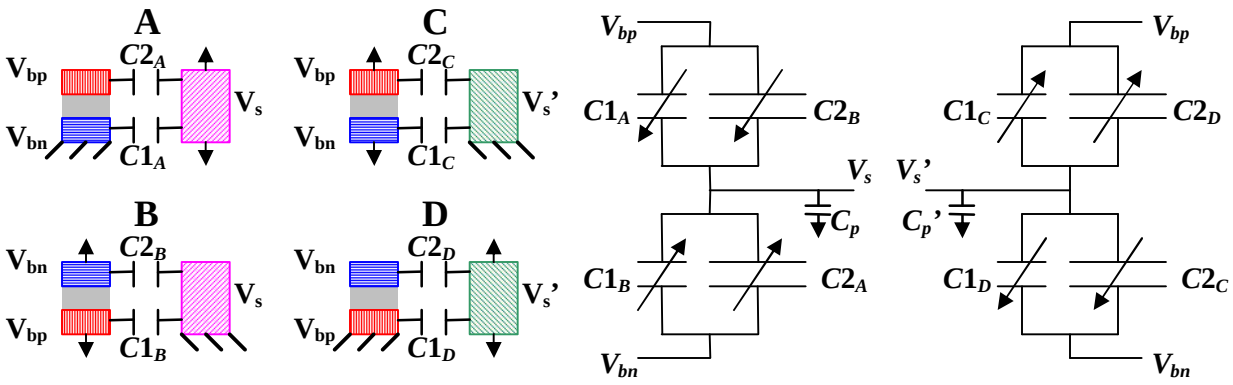

a. Sense Finger Arrangements **b. Balanced Dividers form Full Capacitive Bridge**

Figure III.12 Capacitive Bridge Details

The sense voltages relate to the sense capacitors as

$$V_s = V_b \frac{(C1_A + C2_B) - (C1_B + C2_A)}{C1_A + C2_B + C1_B + C2_A + C_p} \quad V_s' = V_b \frac{(C1_C + C2_D) - (C1_D + C2_C)}{C1_C + C2_D + C1_D + C2_C + C_p'} \tag{3.8}$$

Arrangements A and B connect to one sense output, V_s. Arrangements C and D connect to the second sense output, V_s', which responds opposite V_s to create a differential output. The positive bias voltage, V_{bp}, drives the top of both dividers while the negative bias voltage, V_{bn}, drives the bottom of both.

Each unit of fingers has the layout in Figure III.13a with 20 gaps and 40 individual capacitors. The bias and sense fingers are supported by trusses which are tethered to a device edge (a sensor support, the chip surface, or the paddle). A challenge of the full sensor layout is routing V_{bp}, V_{bn}, V_s, and V_s' to properly connect the terminals of all 24 units and to ensure the proper fingers are mobile. The layout solution routes the four signals along wires around the cantilevered paddle to both sides of each gap. Either the bias or sense side of each unit connects to the paddle to ensure proper mobility per Figure III.12a. Short wires connect the

signals to the appropriate finger truss and terminals in each unit. Regions i through v are indicated for further analysis of parasitic capacitance.

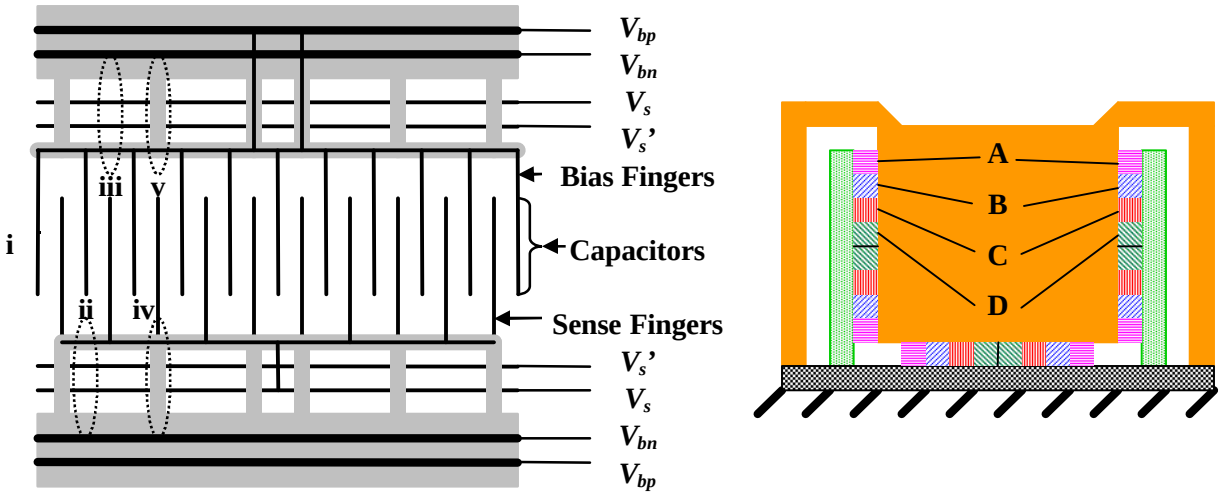

a. Sense Finger Unit Layout with C_p regions **b. Common Centroid Unit Pattern**

Figure III.13 Sense Fingers System Layout Details

The 24 units, six of each arrangement, are placed around the paddle in the common-centroid pattern of Figure III.13b. All six units of each arrangement are wired in parallel. The distributed placement compensates for linear manufacturing variations from either the AMS foundry or CMOS-MEMS post-processing. For example, if the offset between fingers vary linearly from left to right, there are three units of arrangement A with a large offset and three with a small offset. Their parallel combination cancels this variation in offset.

The necessity to route the bias and sense signals around the capacitive bridge creates a large parasitic capacitance on the V_s and V_s' wires. The ideal layout separates all sense wires from other conductors by multiple micron wide air gaps. However, the implemented layout in Figure III.13a shows places where "gray" wires, which are connected to the -2.5 V power supply, and bias wires at dc voltages are near or cross the sense wires. The potential between these constant voltage wires and the sense wires draws charge from the capacitive bridge which decreases the capacitive bridge displacement sensitivity. Models of five characteristic cross-sections across sense wires are presented in Figure III.14 along with their corresponding region of Figure III.13a in parenthesis.

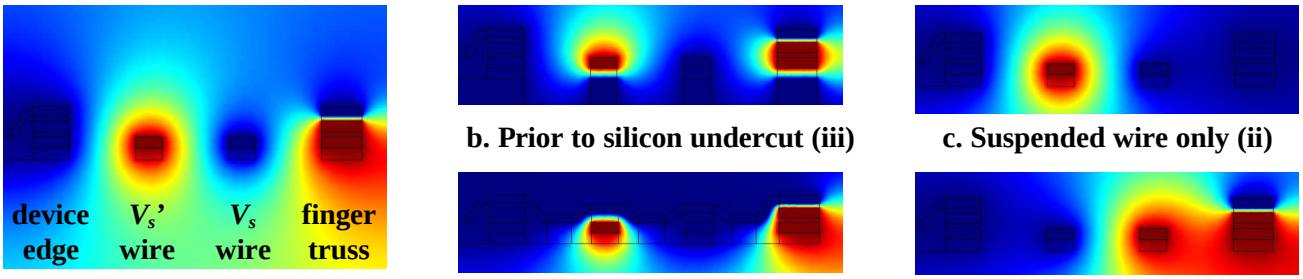

a. Suspended with V_s' truss (iii) **b. Prior to silicon undercut (iii)** **c. Suspended wire only (ii)**

d. Tethered with V_s' truss (v) **e. Suspended with V_s truss (iii)**

Figure III.14 FemLAB Simulations of V_s and V_s' Interconnect Cross-Sections

The red areas are sense wires at 1 V and the blue areas are bias wires at 0 V. Each transition between colors indicates electric field lines which contribute parasitic capacitance from the charge at their ends. Figure III.14a demonstrates the cross-section with the greatest contribution to C_p'. Parasitic capacitance is contributed from "gray" metal 0.4 μm above the *Vs'* wire on its finger truss (on the right side of Figure III.14a) in addition to a smaller capacitance from the isolated V_s' wire. Figure III.14b shows the same cross-section except that the silicon beneath the wires has not been undercut, causing additional abrupt transitions. Figure III.14c shows the ideal cross-section where the only sense conductor is the isolated V_s' wire. Figure III.14d demonstrates the impact of tethering the V_s' wire and the finger truss to the device edge, where a large capacitance to the power supply forms above the V_s' wire. The V_s and V_s' wires have different parasitic capacitance values as shown in Figure III.14e where the V_s wire and finger truss are grouped together producing less parasitic capacitance.

Table III-1 V_s and V_s' Interconnect Parasitic Capacitances (fF) by Region

	V_s, Silicon	**V_s', Silicon**	**V_s, Undercut**	**V_s', Undercut**
Circuit Wiring	126	126	126	126
Fingers (i)	601	601	0	0
Suspended wire only (ii)	352	352	80	81
Suspended with truss (iii)	535	540	313	327
Tethered wire only (iv)	191	191	134	134
Tethered with truss (v)	223	223	162	163
Other regions	487	514	220	248
Total Capacitance	**2515**	**2547**	**1035**	**1079**

All significant geometrical and electrical two-dimensional cross-sections of the V_s and V_s' wires are modeled and summarized in Table III-1 with reference to their region in Figure III.13a. Three-dimensional

effects are neglected to simplify the analysis as the electric field regions corresponding to parasitic capacitance are long compared to their gap width. Circuit wiring capacitance results from interconnect between the wires in Figure III.13a and the amplification electronics. Finger capacitance is between the terminals on the sense fingers and underlying silicon. The tethered wire only region (region iv) not shown in Figure III.14 is the same as region v except the finger truss has all constant voltage wires, eliminating the rightmost transitions in Figure III.14d. The "other regions" capacitance accounts for wires which connect the sense lines along the paddle to those along the sensor supports and chip surface. Removing the silicon below the fingers and sense wires reduces C_p and C_p' by 1480 fF and 1468 fF, respectively. The remaining 1035 fF C_p and 1079 fF C_p' parasitic capacitances reduce the displacement sensitivity of the capacitive dividers determining V_s and V_s' by factors of 7.9 and 8.2, respectively. Failing to remove the silicon decreases the sensitivities by factors of 17.8 and 18.0, respectively.

To drive the capacitive bridge, equal and opposite bias voltages are applied to V_{bp} and V_{bn}. AC bias voltages generate ac sense voltages, V_s and V_s', which are zero when the bias and sense fingers are aligned. Any vertical offset in the fingers will cause the magnitude of V_s to increase and the phase to shift 0° or 180° relative to the bias voltages, depending on the displacement direction. V_s' responds with equal magnitude but opposite phase of V_s. Applying dc bias voltages causes the dc offset of the sense voltages to shift with displacement. Figure III.15a gives the shape of V_s for ±10 μm paddle offsets and Figure III.15b quantifies the displacement sensitivity of V_s in μV/nm as a function of initial paddle offset.

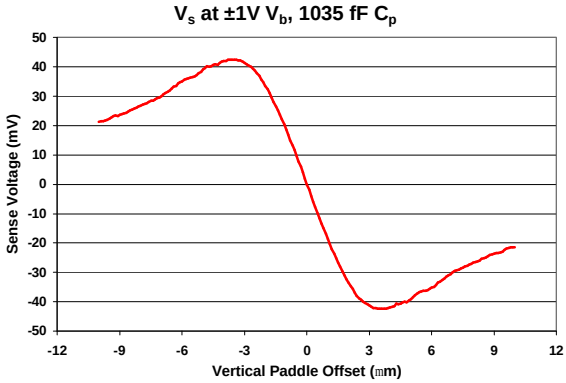

a. Sense Voltage vs. Paddle Offset

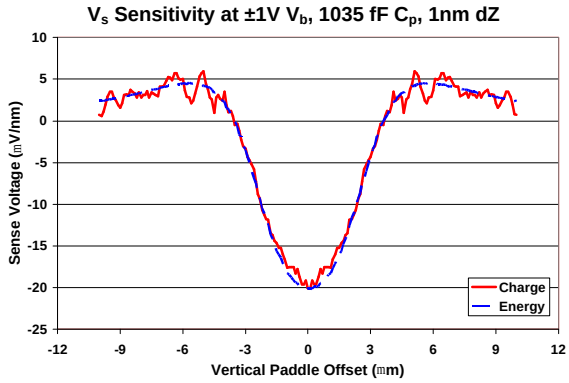

b. Sense Voltage Sensitivity to 1nm Motion

Figure III.15 Bridge Output with Finger Offsets

d. Integrated Electronics

Integrated on-chip electronics detect and amplify the difference between V_s and V_s' before external instruments measure the voltage. This prevents wires that connect the chip to the instruments from increasing C_p and C_p' and decreasing displacement sensitivity. The electronics design on this chip is shared from another project which used a capacitive divider to measure cantilever motion [13].

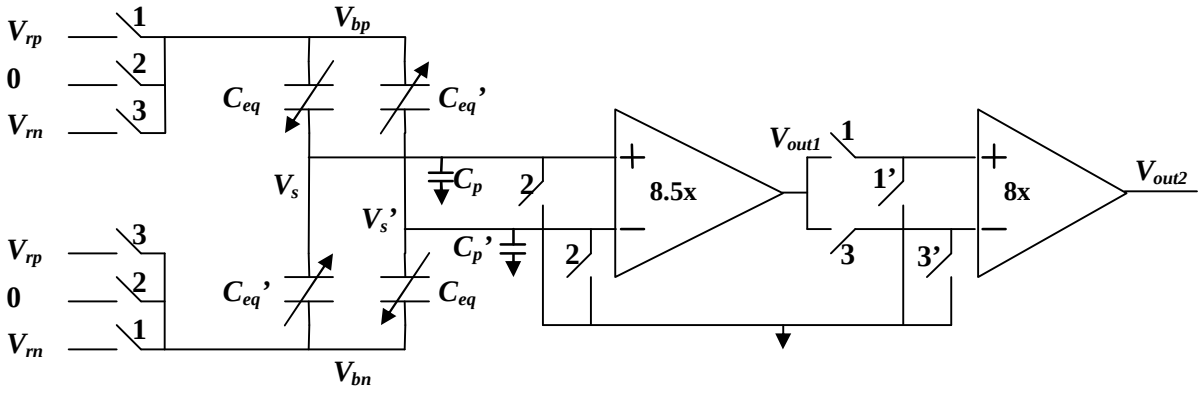

Figure III.16 Integrated Electronics Schematic

Figure III.16 is a schematic of the circuit and switches which amplify ($V_s - V_s'$) 68 times before external equipment captures V_{out2}. The electronics generate three clock signals from an external master clock to route voltages through switches and complete a four-step cycle when measuring cantilever displacement. Figure III.17 demonstrates the circuit function when each clock is active. In Step 1, clock 1 connects V_{bp} and V_{bn}, to external reference voltages, V_{rp} and V_{rn}, respectively. V_s and V_s' connect to a differential amplifier with a gain of 8.5 ($V_{out1} = 8.5\ (V_s - V_s')$). V_{out1} is further amplified by 8 to generate V_{out2}. External equipment is used to measure and record V_{out2}. In Step 2, clock 2 connects all terminals of the capacitive bridge to zero volts to remove built-up charge on the capacitors. V_{out1} is isolated as the floating output from the first amplifier while the inputs to the second amplifier are grounded. In Step 3, clock 3 reverses the bridge voltages ($V_{bp} = V_{rn}$, $V_{bn} = V_{rp}$), the sense voltages propagate through the amplifiers, and V_{out2} is measured again. The second amplifier negates V_{out2} to compensate for the reversed bridge voltages. Step 3 also removes any embedded charge in dielectric materials from step 1. In Step 4, clock 2 connects the bridge terminals and amplifier inputs to zero volts again and the cycle then repeats.

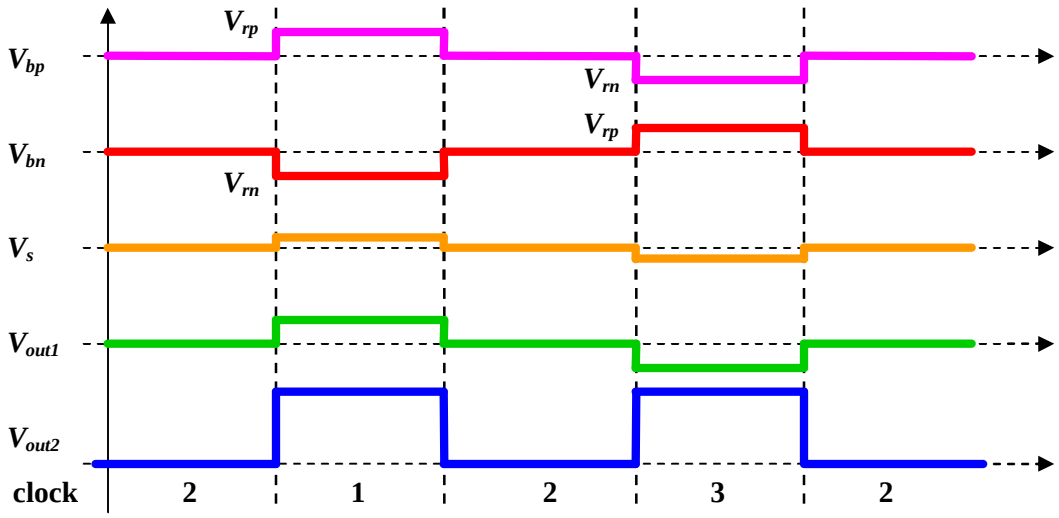

Figure III.17 Circuit Clock Sequence and Signal Development

The 4 step cycle (clock sequence 1→2→3→2 and repeat) prevents leakage charge from affecting the high-impedance voltages, V_s and V_s', for longer than one cycle. The switches in the circuit are designed to not inject any charge onto the capacitive bridge when they switch off. The reset cycles, when clock 2 is active, are necessary because any such stray charge can dramatically impact the output. For example, a stray charge of 19 fC cancels the effect of the paddle moving 1μm.

The combined gain of 68 between the two amplifiers and the differential nature of the first amplifier convert the 20.2 μV/nm displacement sensitivity of V_s and 19.5 μV/nm displacement sensitivity of V_s' to 2.70 mV/nm for V_{out2}. The sensitivity limits vertical paddle displacement to ±1 μm to prevent saturation of V_{out2} when V_r = ±1 V as the electronics can only drive V_{out2} between -2.4 V and 2.4 V. Decreasing V_r to ±0.5 V allows ±2 μm paddle displacement, the maximum displacement for V_{out2} to be linearly dependent on displacement.

IV. Experimental Results

The fabrication and testing phases of the FDNMR chip development are presented in this chapter. First, backside etching is attempted to create the cavity and the resulting membrane by only protecting the perimeter of the critical area underneath the cantilever and capacitive bridge. Second, a backside etching sequence is developed and implemented which completes the cavity by initially patterning the critical area and protecting its perimeter. Third, the detector magnet is machined and mounted onto the silicon chip after which the front-side silicon dioxide and crystalline silicon etches are optimized to release the cantilever assembly. Fourth, the on-chip electronics are tested for functionality and compared to their simulated operation. Fifth, five fabricated chips are tested to measure electrostatic, mechanical, and magnetic excitation of the chip, both for static displacement and resonant motion. The chips follow some or all of the fabrication steps and they demonstrate the complete functionality of chip excitation and force detection. Sixth, the actual capacitive bridge parasitic capacitances are extracted, the displacement noise floor is determined, and the necessary measurement bandwidth is calculated to achieve detection of hydrogen in water with the FDNMR sensor in this work.

a. Open-Area Backside Etching for Cavity

The backside of the chip must be etched to create the front-side silicon cantilever and create a place for the detector magnet, while maintaining the structural rigidity to handle, wirebond, and package the chip. The FDNMR design requires the cavity depth to be 485 μm to make a 50 μm thick cantilever. The cavity must be 1370 μm by 1850 μm to accommodate the cantilever assembly. Etching 50 μm wide, 300 μm deep trenches is a routine process step using DRIE. DRIE is optimized for this narrow gap and high aspect ratio trench geometry, however the resulting trench geometry does not scale to wide, deep trenches [4]. DRIE can etch large open 100 μm deep cavities with vertical sidewalls and a flat bottom.

A nominal DRIE recipe is used to etch a 2 mm by 2 mm wide and 310 μm deep cavity from a 2 mm x 2 mm exposed silicon surface as shown in Figure IV.1. The nominal DRIE process recipe in the Surface Technology Systems (STS) reactor uses a 12 second etch cycle at 22 mT with 130:13 sccm CHF_3:O_2 gas flows [5, 39]. The passivation cycle is 8 seconds long at 11 mT with 85 sccm of C_4F_8 gas flow. An

inductively coupled plasma (ICP) is maintained by a coil carrying 600 W of RF power through the process, and 12 W of RF power is applied through the substrate during etching. After etching, a white-light interferometer measures the depth and bottom surface topography, while the sidewall-angle is determined from a scanning electron microscope (SEM) profile image of the cavity.

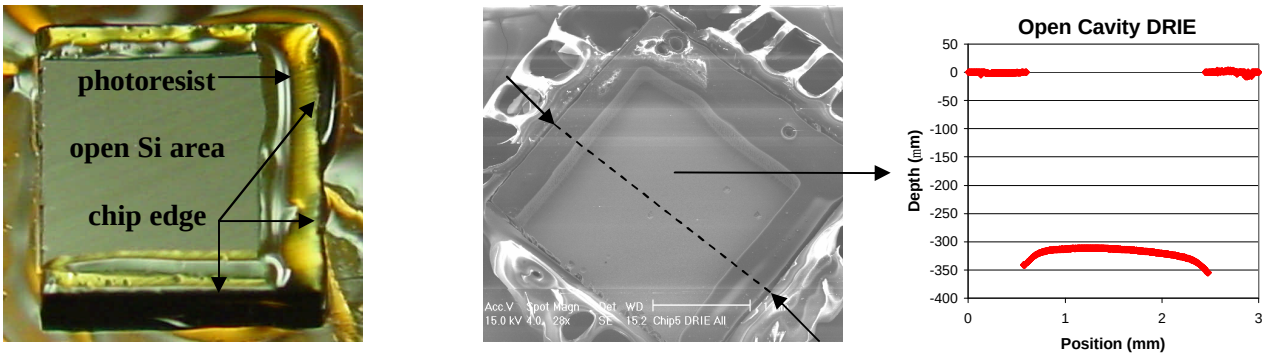

a. hand patterned open area **b. etched cavity in chip** **c. cavity profile**

Figure IV.1 Open-Area Backside Chip Cavity by Nominal DRIE

Figure IV.1c demonstrates problems with the bottom surface uniformity in the nominally etched cavity. The edges of the cavity are up to 44 μm deeper than the center of the cavity. This effect is called edge depth. The sidewalls are also found to undercut at a 7 degree slope upon inspection by SEM, equivalent to a 60 μm undercut at a depth of 485 μm. This undercut region is not readily measurable by an interferometer or profilometer but could extend the steep gradient in depth shown in Figure IV.1c leading to the edges of the cavity. The steep gradient is in the mechanically critical region of both the spring beams and bondpads. A carefully positioned cavity boundary is nominally 80 μm from bond pads in some areas. The cavity boundary position accommodates a generous alignment error of 50 μm to ensure the cavity will form under the entire cantilever assembly. The nominal undercut will approach the bond pads and a misaligned pattern will undercut the bond pads.

Modification of the nominal DRIE process is necessary to etch a cavity with minimal sidewall undercut and zero edge depth. The plasma pressure, substrate RF power, and passivation cycle time are altered to examine their impact on the cavity geometry. The sidewall angle is addressed by protecting the sidewalls during etching and directing the etch reactants vertically. The plasma pressure is increased to promote passivation polymer deposition on the sidewalls. The associated rise in etch pressure will also increase ion scattering to etch the sidewalls but that effect is minimal since the mean free path is roughly 2.5

mm. The substrate RF power is increased to draw the ions vertically to the substrate by ballistic transport across the plasma sheath. The cause of edge depth is hypothesized as silicon etch-lag in the center due to excessive passivation polymer deposition. Extra polymer is deposited in large cavities since the C_4F_8 plasma can dip into such cavities [6]. The passivation cycle time is reduced to combat this polymer buildup and the resulting edge depth.

Table IV-1 Open-Area DRIE Experiments

Recipes	Etch : Passivate Pressure	RF Power	Passivation Time	Cavity Center Depth	Sidewall Angle	Edge Depth
Nominal	22 mT : 11 mT	12 W	8 s	190 μm	7°	3.5 μm
Exp. 1	22 mT : 11 mT	12 W	7 s	190 μm	7°	3 μm
Exp. 2	22 mT : 11 mT	12 W	6 s	190 μm	8°	2.5 μm
Exp. 3	22 mT : 11 mT	12 W	5 s	210 μm	9°	1.5 μm
Exp. 4	22 mT : 11 mT	12 W	4 s	210 μm	11°	1 μm
Exp. 5	25 mT : 13 mT	12 W	6 s	210 μm	7°	2 μm
Exp. 6	25 mT: 13 mT	15 W	6 s	250 μm	4°	3.5 μm
Exp. 7	22 mT : 11 mT	15 W	6 s	210 μm	6°	3 μm
Exp. 7b	22 mT : 11 mT	15 W	6 s	410 μm	9°	7 μm

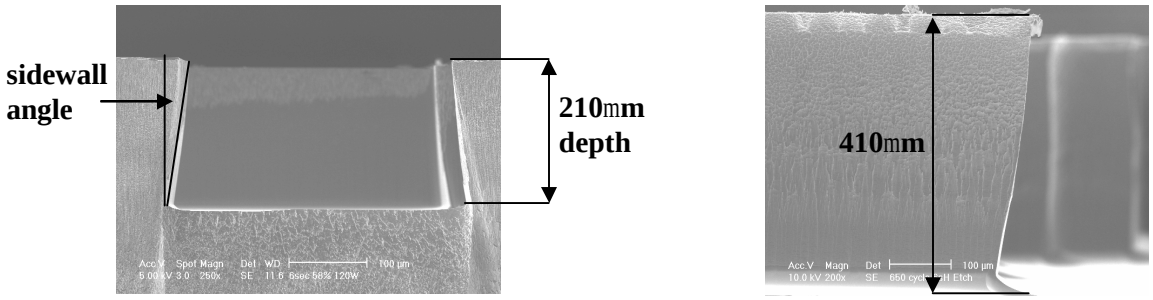

a. Exp. 5 **b. Exp. 7b**

Figure IV.2 Open-Area DRIE Experiment Measurement Images

Combinations of the three variables did limit the sidewall angle or edge depth, but no recipe was found to constrain both as shown by Table IV-1. Experiment 7 with 15 W substrate RF power and a 6 second passivation cycle time was etched down to 410 μm and both the sidewall angle and edge depth increased to large levels. Open cavity DRIE cannot etch a flat bottom, constrained cavity 485 μm into a silicon surface.

b. Patterned-Area Backside Etching for Cavity

The cavity etching challenge is solved by patterning the backside with photoresist prior to etching. However, this is difficult to accomplish as the chips are diced prior to post-CMOS processing. The wide avity area is patterened into smaller neighboring regions for high aspect ratio etching. The divisions between regions are removed by a slight undercut inherent to DRIE to create a deep, uniform, low aspect ratio cavity.

To coat with photoresist and pattern the backside, a FDNMR chip is placed on a two inch wafer, front-side down, halfway from center to edge of the wafer, with the intended cavity region towards the wafer edge. A second piece of silicon is placed against the outer chip edge. The chip and the second silicon piece are secured to the two inch wafer using photoresist to achieve a flush top surface and minimal gap along their adjoining edge. The second piece of silicon is the same thickness as the FDNMR chip but larger in area and it draws the outer edge bead of photoresist off the smaller FDNMR chip during photoresist spinning. After HMDS treatment, AZ4400 photoresist is applied to the surface of the two silicon chips and the surrounding region. The whole two inch wafer is spun at 5000 rpm to thin the photoresist to three microns and allowed to dry on a 90 C hotplate for 45 seconds. It is important to slowly ramp the spin speed up and down over 10 seconds each to prevent edge bead formation on the side edges of the FDNMR chip. The resulting film is a thin but uniform seed layer of photoresist. An additional five microns of AZ4400 is spun on at 3000 rpm by the same application process and this resist stack is baked on a 90 C hotplate for 90 seconds. The second coating does have has a 1.5 μm thickness gradient but the total gradient is 50% smaller than depositing a single eight micron layer of photoresist. The photoresist layer is now patterned by 10 W/cm^2 ultraviolet light shown through a chrome on glass mask for 35 seconds. The pattern is developed in a 3:1 de-ionized water:AZ400T solution for 45 seconds, rinsed gently, and allowed to dry under a chem-wipe towel. The towel absorbs any photoresist particles suspended in the rinse water. An oven bake at 90 C for 15 minutes and 120 C for 15 minutes completes the patterning.

To achieve a uniform cavity bottom, photoresist patterns from several masks are investigated. The photoresist patterns extend 70 μm beyond the cantilever structure, as shown in Figure IV.3a, to accommodate 50 μm alignment errors in any direction. The first set of tested patterns share the crosshatch pattern in Figure IV.3b. Separate patterns have region divisions from 5 μm to 10 μm, and etch region squares from 25 μm to

50 μm on a side. When using the patterns on blank pieces of silicon, the resulting center cavity etch depths after 300 minutes of nominal DRIE vary from 340 μm to 500 μm, with edge depths from 21 μm to 32 μm. The larger hole patterns promote faster etching since the mass transport rate of reactants is higher. The silicon located below division intersections is difficult to etch away to complete a flat cavity surface. The passivation plasma can not dip into the cavity so the edge depth is reduced, though still unacceptable for a 50 μm thick cantilever. The edge depth problem is now caused solely by fresh reactants diffusing from areas around the cavity boundary. These new reactants increase the edge etch rate as a micro-loading effect, leading to etch lag in the center. The pattern in Figure IV.3c decreases the area of the boundary etch regions. The dimensions shrink from 50 by 50 μm to 48 by 50 μm to 40 by 48 μm to reduce the mass transport rate of reactants. The edge depth is reduced to 8μm in a 370μm deep cavity after 200 minutes of etching. Unfortunately, a photoresist pattern more than 12 μm thick is necessary to mask the divisions while etching down 485 μm as the silicon etch rate decreases in deep trenches. 8 μm is the maximum photoresist thickness achieved to evenly pattern a chip, since the thickness variation from spinning must be equal or less than 1.5 μm. More variation causes developed patterns to change line-width across the cavity region. This induces different etch rates and a etch depth gradient across the final cavity.

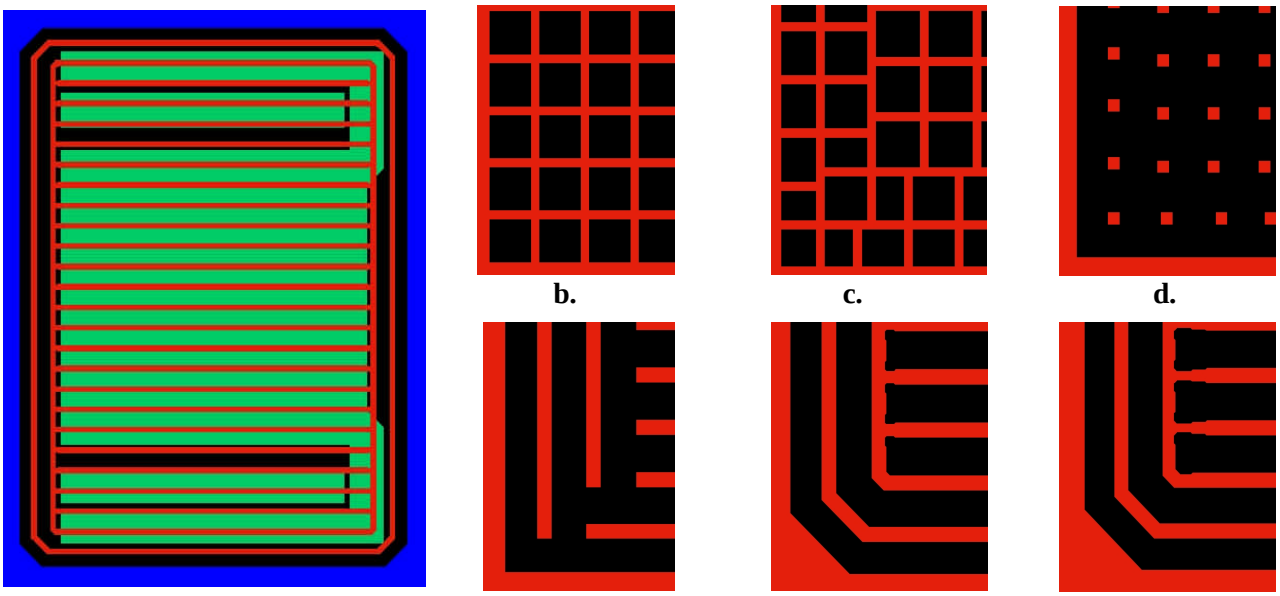

Figure IV.3 Backside Mask Development

The slow etch rate and resulting 12 μm thick photoresist requirement of the crosshatch patterns is solved by opening up the pattern to allow more reactants from the plasma into the cavity. Square dots in Figure IV.3d, 100 μm^2 in area, improve the etch rate but they don't effectively limit mass transport of new reactants. It is also difficult to achieve 100% yield of the dot pattern as they easily detach from the silicon surface during development. A single absent dot will increase the local etch rate by 10%. Larger, more adhesive dots leave spikes on the cavity bottom surface. The spikes cause irregular spring-beam bending and disrupt the attachment of the magnet to the etched surface. The compromise is a set of 20μm wide divisions arrayed across the cavity to divide it into trenches. Initial designs similar to Figure IV.3e have divisions to protect the edges and separate divisions to fill the interior. The spacing between divisions decreases toward the boundary, from 50 μm to 48 μm to 42 μm to eliminate edge depth. The gap between the horizontal middle and vertical boundary divisions causes 20 μm trenches in the surface of a 400 μm deep cavity because of the open nature of these regions. The design Figure IV.3f closes the gap and reduces the surface area of division intersections to prevent residual spikes on the final cavity surface. Figure IV.3g is the final design where the interior divisions gradually narrow towards the boundary region. The etch regions widen from 50 μm to 54 μm to increase vertical mass transport since reactants can only laterally enter the box-canyon regions from one side resulting in a decreased local etch rate. The boundary region divisions which create the box-canyons also narrow from 20 μm to 19 μm to encourage their complete removal during the etching process. The complete final pattern is shown in Figure IV.3a overlaid on the cantilever structure with nominal alignment.

The walls of silicon remaining under the divisions must be removed when the individual trenches have etched to the final depth. The initial trench etch DRIE recipe is a 90 minute nominal process recipe with 20W of substrate RF power to etch 230μm deep trenches. The plasma pressure is then reduced to 19 mT : 9 mT (etch : passivate) to promote sidewall undercut by depositing a thinner layer of conformal passivation polymer. When the cavity is more than 400 μm deep the photoresist mask is etched away. Around 450 μm, the network of silicon walls are undercut. The internal walls eventually etch away in the DRIE plasma, leaving an open flat cavity. Figure IV.4a is an interferometric map of the final bottom surface, where the

uniform color indicates an edge depth within 5µm and an average etch depth of 495µm after 220 total minutes of etching. This depth is actually 505µm, measured by a stylus profilometer, leaving a 30µm thick silicon membrane. The measured profile in Figure IV.4b shows a flat surface, no x-direction tilt and only slight y-direction curvature from the box-canyon effect.

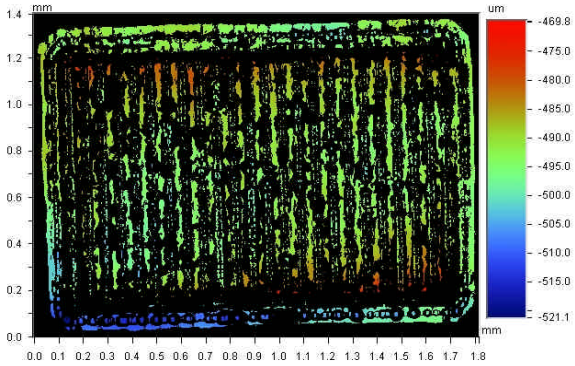

a. bottom surface topography

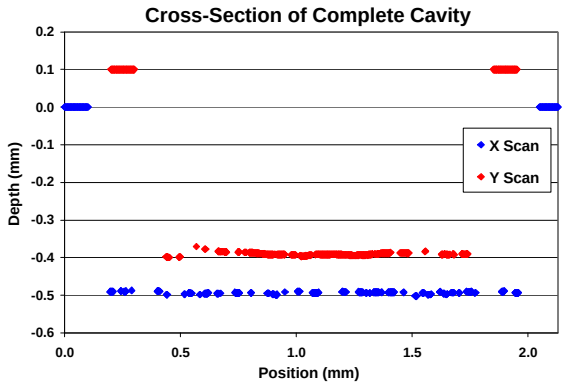

b. bottom surface profile

Figure IV.4 Completed Cavity Topography and Profile

A SEM image of the chip is also shown in Figure IV.5a. Some division intersection spikes and wall flakes do remain, but these are gently brushed away before further processing. Additional photoresist is painted on around the perimeter of the cavity after the initial 90 minute etch to thoroughly protect the backside surface. The painting can not precisely protect the whole surface without damaging the delicate division pattern and initial cavity. The irregular final cavity boundary indicates areas where the painted photoresist did not protect the backside and the edges were etched.

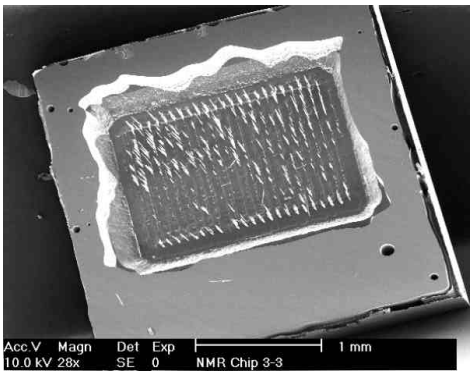

a. SEM view of cavity

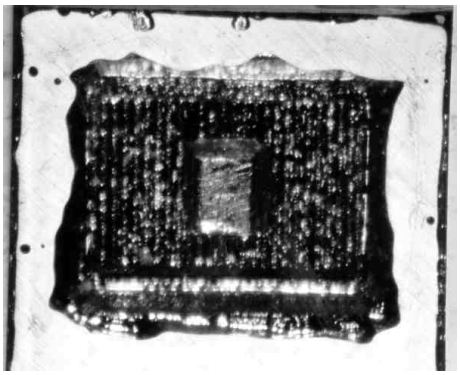

b. Magnet mounted into cavity

Figure IV.5 Completed Cavity View and Chip with Attached Magnet

c. Magnet Assembly and Frontside Release Etching

The detector magnet design calls for a 750 μm diameter 250 μm thick nickel disk. The actual machined magnet is a truncated cube, 600 μm on a side and 250 μm thick. The nickel detector magnet is made by cutting a 600 μm wide sliver from a 250 μm thick foil sheet of 99.99% pure nickel. The sliver is sliced into squares which have 82% of the mass of a 750 μm diameter disc. A small drop of 3M^{TM} super-glue gel is dabbed onto the center of the backside cavity. Any FDNMR signal generated by hydrogen atoms in the glue must be systematically subtracted from the measured signal of a sample. Magnetic tweezers position the nickel magnet onto the glue drop and gently press it into the glue resulting in the cavity and magnet assembly of Figure IV.5b. After allowing the glue to dry several hours, a brief 10 minute, 150 W, 50 mT O_2 plasma removes the thin glue residue which coats the cavity surface as the glue vapors settle.

The remaining etch release of the top surface is similar to previous work on CMOS-MEMS [16, 36, 39]. CF_3^- ions in the CHF_3:O_2 plasma of a PlasmaTherm 790 reactor anisotropicly etch silicon dioxide not covered by aluminum to expose the cantilever and capacitive bridge structures. The plasma has 100 W of RF power while CHF_3 and O_2 gasses flow at 22.5 and 32 sccm. The plasma pressure is 125 mT for 140 minutes and 100 mT for 10 minutes. The etch makes trenches down to the silicon surface. Next, a 30 minute, 10W substrate RF power, 6 second passivation cycle time DRIE extends the trenches through the silicon membrane to pattern the cantilever assembly in Figure IV.6a. The etch results in the silicon trenches with a slight undercut. Trenches, two microns and wider, extend through the membrane and the V_s and V_s' wires are undercut. A final 10 minute DRIE increases the RF power to 20 W to complete the cantilever release by driving reactants into trenches where silicon still remains. Figure IV.6a demonstrates some capacitive bridge gaps which are cleared by this last high-power etch. A careful inspection of the final gaps reveal a few 0.1 μm wide residual stringers of polymer or silicon dioxide from the CHF_3 etch. Incomplete oxide etching or interactions between the plasma and the aluminum mask are possible sources of the stringers. The stringers are assumed small enough to not impact the spring constant or resonant performance of the cantilever.

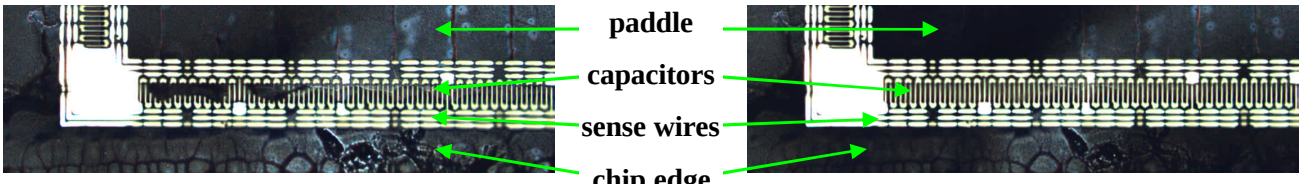

a. 30 minute DRIE 10 W etch **b. After extra 10 minute 20 W etch**

Figure IV.6 Final Silicon DRIE Release, Backside View of Paddle Perimeter

The complete fabrication of the cavity and the release of a 30 µm thick cantilever results in capacitor vertical misalignment between 0.5 µm and 2.0 µm as measured using interferometry and shown in Figure IV.7a. The average offset is within the 2 µm offset limit of the capacitive bridge. The common-centroid sensor layout compensates the variation in offset to maintain a balanced capacitive bridge.

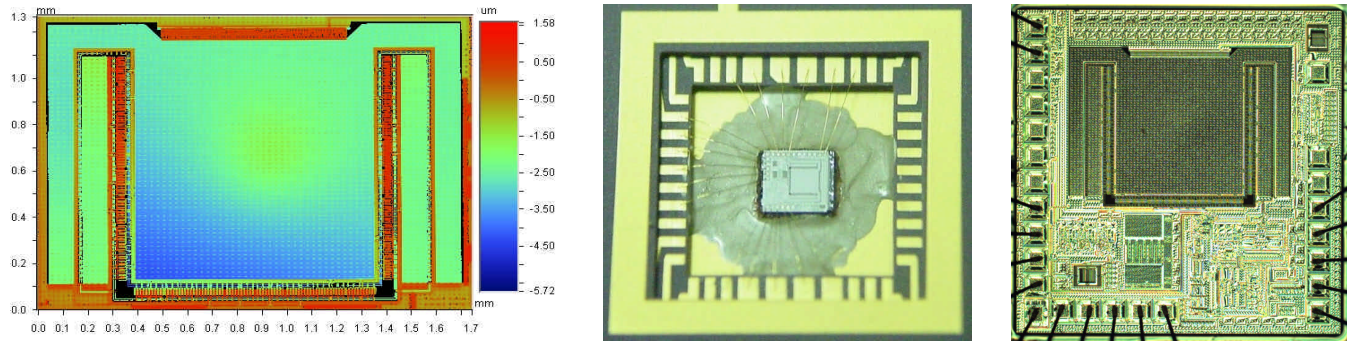

a. Surface topography of released chip **b. Packaged and wirebonded chip** **c. Chip close-up**

Figure IV.7 Front-Side of Fabricated of FDNMR Chip

d. Integrated Electronics Testing

With fabrication completed, FDNMR chips are secured with silver paste into a ceramic package and wirebonded with gold wire as shown in Figure IV.7b. The cantilever and wirebonds are clearly visible in Figure IV.7c. Table IV-2 below outlines the parameters of 5 packaged chips which together provide the experimental results of electronic, mechanical, and magnetic testing through the remainder of this chapter.

Table IV-2 Packaged FDNMR Test Chips, all are frontside etched

Chip ID	Backside Etched	Si Thickness	Ni Magnet	Comments
A	No	-	-	clock and amplifer electronics tests
B	Yes	60 µm	No	self-test actuation test
C	Yes	60 µm	No	physical probe test
D	Yes	30 µm	Yes	static magnet, linearity, and noise tests
E	Yes	30 µm	Yes	acceleration and magnetic resonance tests

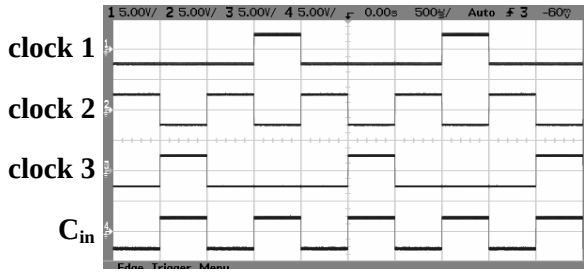

a. Clock waveforms

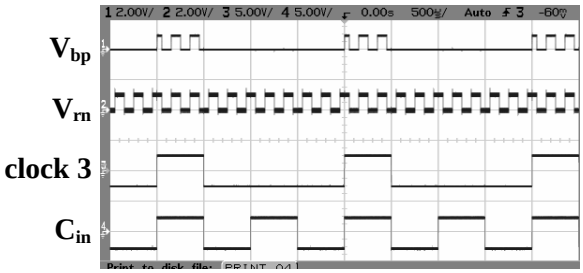

b. Reference signal propagation to bridge

Figure IV.8 Clock Signal and Switch Functionality, Chip A

Testing the electronics begins by applying ±2.5V to the chip power supplies. A 5 Vpp (peak-to-peak voltage) 1 kHz square wave drives the master clock input, C_{in}, to generate the three clock signals recorded in Figure IV.8a. Next, a 1.0 Vpp, 0.5 V offset, 5 kHz square wave is applied to the reference voltage, V_{rn}. V_{rn} propagates to V_{bp} on clock 3 in Figure IV.8b. The propogation test is repeated for all combinations of clocks, reference voltages, and bridge voltages with success. The amplifiers are characterized for input offset voltage and gain in Figure IV.9a by driving the zero micron offset capacitive bridge in Chip A with ±1 V V_r during clock signals 2, 1, 2, 3, and 2. The gains of 8.5x and 8.0x for the first and second amplifiers are defined by polysilicon resistor ratios so they are assumed to be accurate for initial analysis. Mismatch between the internal branches of the differential amplifiers cause an output voltage even when the inputs are all zero volts during clock 2. This is modeled as an input voltage on the positive amplifier terminal. Mismatch between C_p on V_s and C_p' on V_s' cause a small output response during clocks 1 and 3. The measured values of C_p and C_p' can not be calculated from electronic testing results but they are determined following mechanical testing of the sensor.

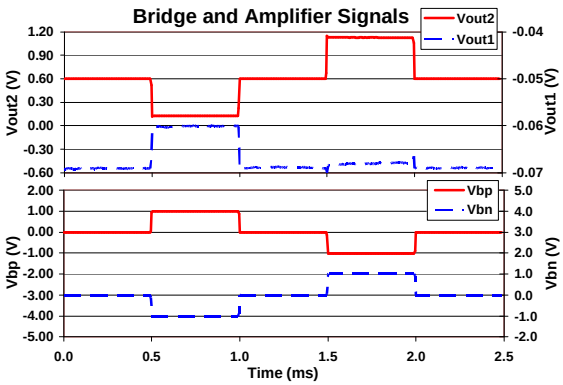

a. Amplifier output with 0 mm offset, ±1 V V_r

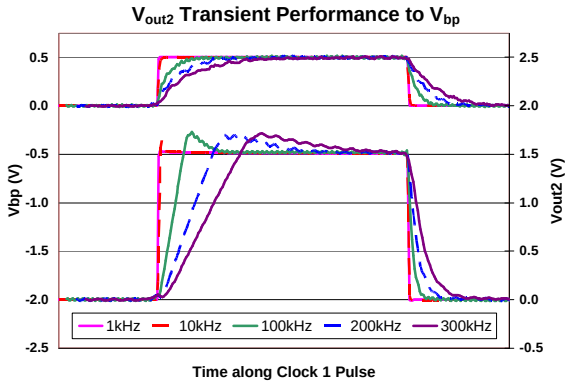

b. V_{out2} response to high frequency C_{in}

Figure IV.9 Amplification Electronics Functionality and Speed, Chip A

The input offset voltage from the first amplifier, V_{os1}, is -8.1 mV since V_{out1} = 8.5 * V_{os1} = -69mV during clock 2. The input offset voltage from the second amplifier, V_{os2}, is 75 mV since V_{out2} = 8.0 * V_{os2} = 600mV.

$$V_{out2,clock1} = 8.0(8.5(V_s + V_{os1} - V_s') + V_{os2}) = 8.0(V_{out1} + V_{os2}) \quad (4.1)$$

$$V_{out2,clock3} = 8.0(V_{os2} - 8.5(V_s + V_{os1} - V_s')) = 8.0(V_{os2} - V_{out1}) \quad (4.2)$$

By considering V_{os2} and the clock 1 and clock 3 responses of V_{out1} and V_{out2}, the second stage amplification is measured at 7.90 and 8.27 using Equations 4.1 and 4.2 where the 8.0 factor is the unknown. This analysis is self-consistent because the assumed gain of 8.0 used to determine V_{os2} is similar to both 7.90 and 8.27. It is necessary to directly measure V_s and V_s' directly to confirm the 8.5x gain of the first amplifier but these voltages are not available to minimize C_p and C_p'. However, the first and second amplifier resistors do share similar geometries so the first amplifier gain can be assumed accurate at 8.5 as designed since the 8.0 gain of the second amplifier is verified.

The bridge response time and electronics bandwidth is tested by increasing the C_{in} clock frequency to determine the measurement bandwidth of the system and the maximum frequency where V_{out2} settles at a DC value for measurement. Figure IV.9b shows V_{bp} (top) and V_{out2} (bottom) during the half-period when the bridge signals are propagated through the amplifiers for C_{in} clock frequencies from 1 kHz to 300 kHz. The rise time of the 300 kHz V_{out2} signal is 0.5 μs, as limited by the a 1 MHz bandwidth of the oscilloscope used to capture the time-domain waveform. The 200 kHz V_{out2} signal settles in 1.5 μs leaving a 1 μs stable voltage before the clocks set the bridge terminals to zero volts. 200 kHz is the maximum C_{in} clock frequency allowed by the measurement electronics for electronic detection of cantilever displacement.

e. Induced Motion and Excitation Detection Results

The FDNMR chip is driven and can sense force by several methods. Simple tests move the cantilever to a new constant position with electrostatic, mechanical or magnetic force. Magnetic and acceleration forces are used to test the dynamic functionality of the sensor and verify its resonant frequency.

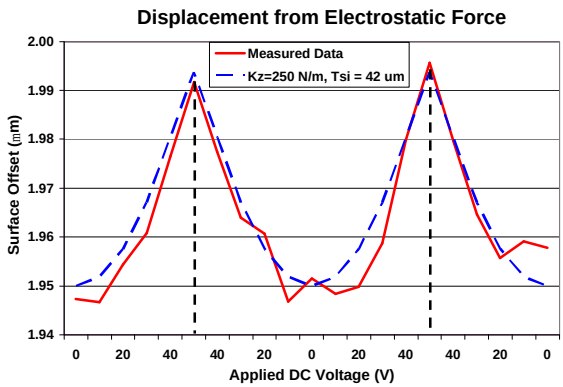

a. Displacement from DC Self-Test, Chip B

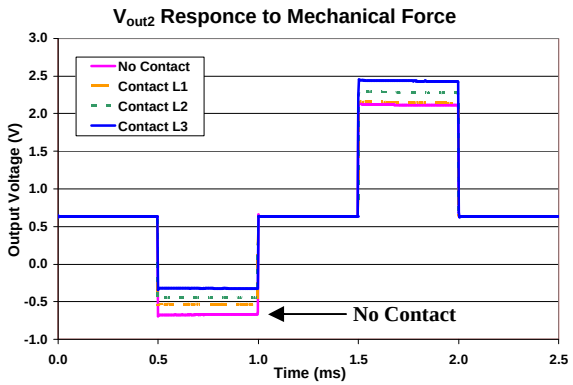

b. V_{out2} response to probe on cantilever, Chip C

Figure IV.10 Static Electrostatic and Physical Displacement Tests

To generate electrostatic force, a DC voltage is applied between the self-test terminals of a released chip. Physical deflection is measured using an interferometer and plotted in Figure IV.10a as the voltage is ramped twice from 0V to 48 V and back to 0V. The resulting 46 nm displacement confirms the release of the chip and successful actuation. The 1.95 μm offset is the result of the released cantilever curling. The tested chip, Chip B, has a 60μm thick cantilever with an expected deflection of 16 nm. However, the 46 nm measured deflection matches a 42 μm thick chip with a 250 N/m free-ended cantilever spring constant considering the self-test capacitance from Figure III.9a. An explanation for the difference between measured and extracted thickness is not clear. The free-ended cantilever model, which has four times more flexiblity than the guided-end models developed in Figure III.5, is appropriate because the cantilever is not constrained to remain parallel to the chip surface during self-test actuation.

Mechanical force is applied to Chip C by gently depressing the cantilever with a micro-manipulator. The capacitive bridge and electronics detect and measure the displacement since V_{out2} responds monotonically positive with applied mechanical force in Figure IV.10b. The micro-manipulator does not touch the cantilever for the no contact case, and applies increasing force on the cantilever from contact level 1 (L1) through contact level 3 (L3). The forces are not quantitative but the output response does confirm electronic detection of physical cantilever displacement.

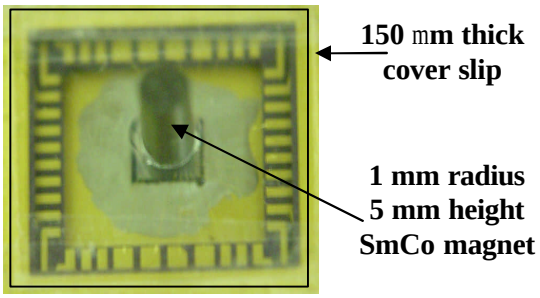

a. Static magnetic force setup

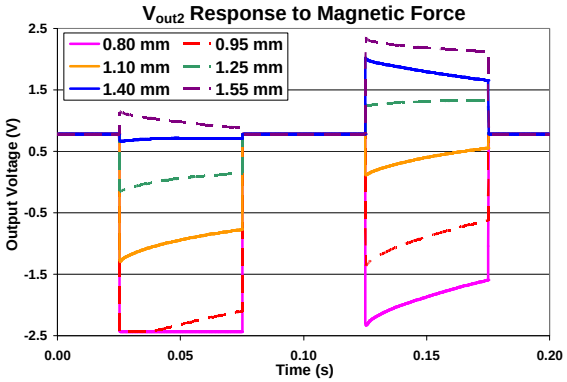

b. Sensor response to magnetic force, Chip D

Figure IV.11 Static Magnetic Force Test

A static magnetic force is applied to the cantilever on Chip D by suspending a permanent Samarium Cobalt (SmCo) magnet above the chip on a 150 µm thick glass cover slip as shown in Figure IV.11a. The SmCo magnet magnetizes and attracts the nickel magnet on the cantilever with a force proportional to $1/r^4$ where r is the distance between the magnets. Placing a single cover slip between the package and magnet (0.8 mm separation between magnets) results in a negative V_{out2} nearly saturating the electronics at -2.3 V during clock 3 in Figure IV.11b. Inserting additional cover slips gradually increases V_{out2} as the cantilever experiences less displacement from the larger distance between magnets. The non-linear effect of magnet position on V_{out2} is characteristic of the non-linear force dependency on distance. V_{out2} indicates greater displacement per each 150 µm of SmCo magnet position change as the SmCo magnet is brought closer to the cantilever.

The settling of V_{out2} towards 0.6V in Figure IV.11b is the result of charge on V_s and V_s' leaking off these high impedance circuit nodes and returning V_s and V_s' to 0V. The leakage path has an approximate time constant of 75 ms, and a resistance of 75 GO if C_p and C_p' are assumed to be 1.0 pF. The leakage is evident in Figure IV.11b because the electronic signal continues for 50 ms.

The FDNMR chip successfully responds to constant electrostatic, physical and magnetic forces. Chips D and E are tested for their dynamic response to acceleration and magnetic forces. Chip D is mounted to a vibration table as shown in Figure IV.12a to measure its response from sinusoidal acceleration forces. An oscillating 1 G, 9.8 N/m, magnitude acceleration is applied from 1.5 kHz to 8.0 kHz. V_{out2} in Figure IV.13a indicates a resonant frequency at 3.32 kHz with several smaller and less defined peaks at higher frequencies.

The test platform for the acceleration test is not completely rigid which introduces noise and extra resonant peaks into the acceleration measurement.

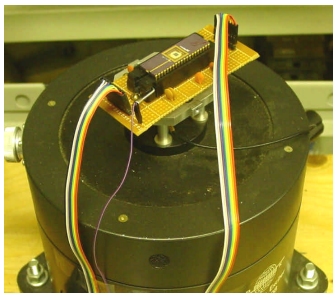

a. acceleration force setup

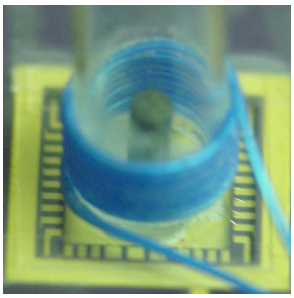

b. magnetic mini-coil

Coil Specifications:

3.9 mm radius
4 mm height
9 turns

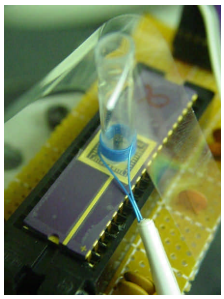

c. magnetic force setup

Figure IV.12 Test Setups for Dynamic Acceleration and Magnetic Testing

To verify the measurement, the SmCo magnet is again positioned above Chip D on a cover slip to magnetize the nickel on the cantilever. A small coil is secured around the SmCo magnet above the chip, as shown in Figure IV.12c. A 1.0 A magnitude AC current drives the coil to generate a 13.6 gauss oscillating B-field across the nickel magnet, with a gradient of 2.3 gauss/mm. V_{out2} indicates resonant cantilever oscillations at 3.63 kHz (Q = 16, parallel motion to chip surface) and 4.70 kHz (Q > 100, tortional motion to chip surface). The vertical cantilever resonant frequency is 3.63kHz as this roughly corresponds to the acceleration force test. Differences in the force distribution can account for discrepancy between acceleration and magnetic resonant frequency. The mechanical model for a 30 µm thick cantilever and 250 µm thick magnet predict a 3.0 kHz resonant frequency. The rough agreement between the model and experimental data supports the model for design of the sensor and analysis of results.

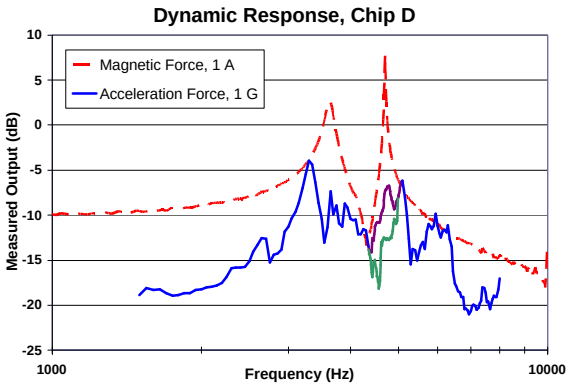

a. dynamic force response, Chip D

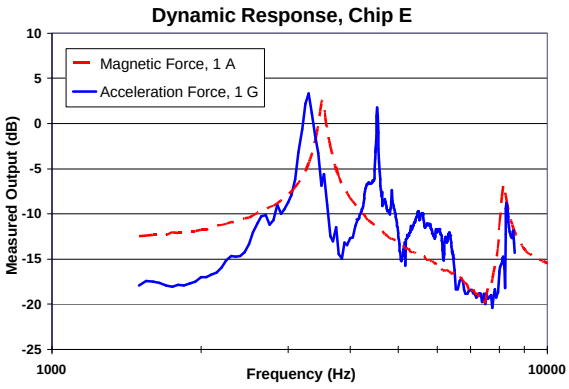

b. dynamic force response, Chip E

Figure IV.13 Dynamic Force Tests to Detect Resonance, V_r = ±1 V

The response of Chip E is also tested with dynamic acceleration and magnetic forces. The results in Figure IV.13b indicate a resonance at 3.52 kHz (Q = 20) from magnetic force similar to the 3.28 kHz resonance shown from external acceleration. Chip E is more sensitive than Chip D to acceleration force at resonance as 1 G generates a 2.34 Vpp V_{out2}, while Chip D only generates a 0.42 Vpp V_{out2}. The strong acceleration response and widely separated, distinct resonant peaks of Chip E indicate it is completely released and demonstrates resonant motion as designed.

f. Measured Data Analysis

Quantitative analysis of the measured force versus output voltage data allow determination of the parasitic capacitance values, their imbalance and the resulting noise floor of the system in detecting resonant motion at atmospheric pressure.

The 1 G acceleration, A_m, applied to Chip E applies a known force to the cantilever, considering its effective mass. The displacement of the cantilever, d_z, is found using Equation 4.3.

$$F_m = m_{eff} A_m = \frac{k_z d_z}{Q} \tag{4.3}$$

Chip E has a 30 µm thick cantilever and a 250 µm thick magnet, giving it a m_{eff} of 0.85 mg and a k_z of 371 N/m. The measured Q is 20. The vertical displacement is thus 0.46 µm. The displacement causes a 2.34 Vpp V_{out2} signal when C_p and C_p' are both 1.12 pF to match the measured data at resonance. 1.12 pF is 63 fF larger than the average of C_p = 1.035 pF and C_p' = 1.079 pF predicted by simulation. The three-dimensional effects ignored by simulation can account for this difference.

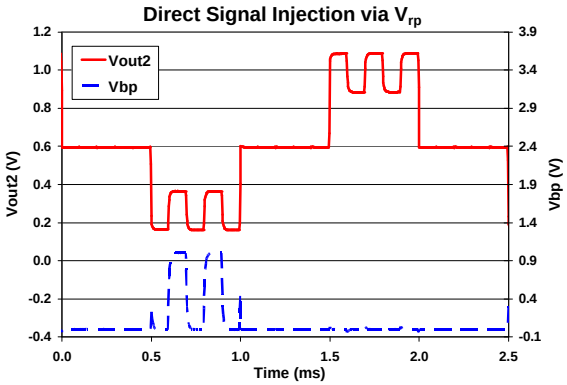

a. Full cycle induced bridge voltage, Chip A

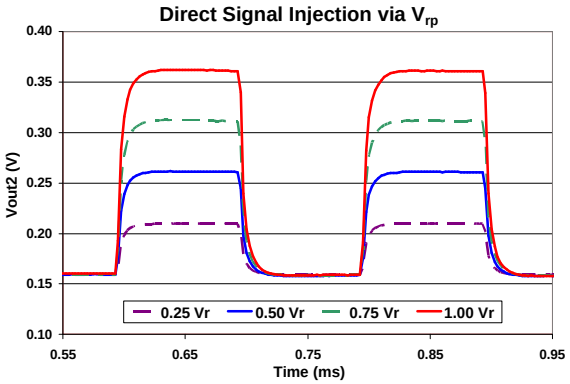

b. Clock 1 induced bridge voltage, Chip A

Figure IV.14 C_p Inbalance Extraction by Unequal Bridge Voltages

The measured imbalance between C_p and C_p' is extracted by driving V_{bp} while setting the V_{bn} to zero volts during clock 1, and vice-versa during clock 3. Figure IV.14a demonstrates the resulting impact on V_{out2} where C_p is smaller than C_p'. A detailed view of the clock 1 period V_{out2} signal with multiple amplitudes of V_r is shown in Figure IV.14b. Equation 4.4 relates the complete capacitive bridge to V_{out2} ignoring the offset voltages, where the $C_p = C_t - C_i$, $C_p' = C_t + C_i$.

$$V_{out2} = 68\,V_r\left(\frac{C_{eq}}{C_{eq}'+C_t-C_i}-\frac{C_{eq}'}{C_{eq}'+C_t+C_i}\right) \tag{4.4}$$

The vertical offset is assumed to be zero microns, $C_{eq} = C_{eq}' = 75$ fF from the model in Figure III.11b, and C_t = 1.12 pF as a placeholder for equal C_p and C_p'. The imbalance capacitance, C_i, is 29 fF, making C_p = 1.091 pF and C_p' = 1.149 pF. This 59 fF imbalance is 15 fF larger than to the 44 fF imbalance predicted from simulation. The close match between modeled and measured C_p and C_p' confirm the electrical model of the sensor.

With the actual parasitic capacitance determined, the true relation between displacement and V_{out2} is presented in Figure IV.15. The maximum sensitivity of V_{out2} to 1 nm of displacement is 2.56 mV.

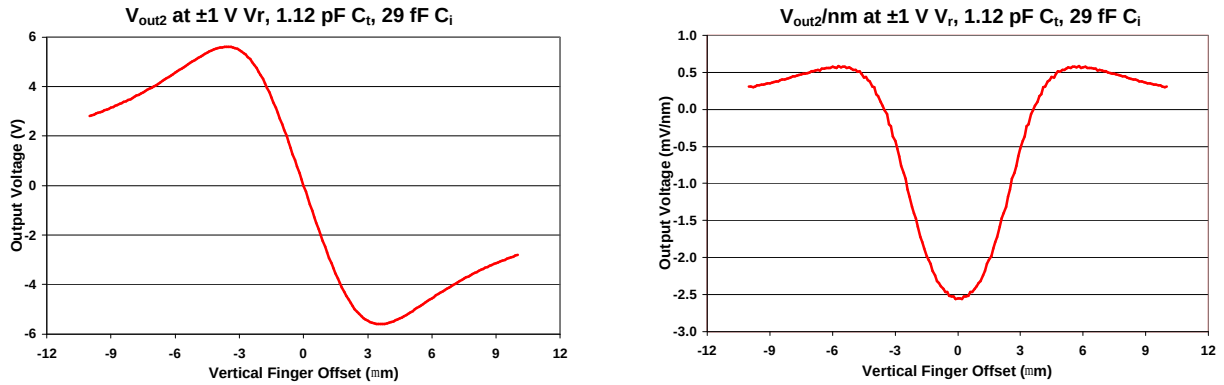

a. V_{out2} vs. Displacement **b. Sensitivity in V_{out2} / nm**

Figure IV.15 Transduction Performance with Measured Parasitic Capacitances

The displacement noise floor of the sensor is determined by reducing the coil current to ensure linearity in sensor performance and to find the point where SNR = 1. The cantilever on Chip D is driven into resonance using the SmCo magnet and coil with currents from 1 A_{rms} down to 3 mA_{rms}. This corresponds to B-field gradients across the nickel magnet of 3.3 gauss/mm down to 0.01 gauss/mm. The V_{out2} signal is linear with coil current when V_{out2} is an order of magnitude above the noise floor, 2.25 mV in Figure IV.16a. 32

waveform measurements of a 3 mA_{rms} excitation signal are averaged to a 4.9 mV signal and 2.25 mV of noise. The 32 averages reduce the noise bandwidth from the 1 MHz measurement bandwidth to 31.3 kHz. The 2.18 SNR can be improved by raising the number of averaged waveforms to 128 (7.8 kHz noise bandwith) and 512 (1.95 kHz noise bandwidth) as shown in Figure IV.16b. Each step improves SNR by 1.7, similar to the factor of 2 improvement expected from increasing the averaging by 4 and decreasing the noise bandwidth by 4.

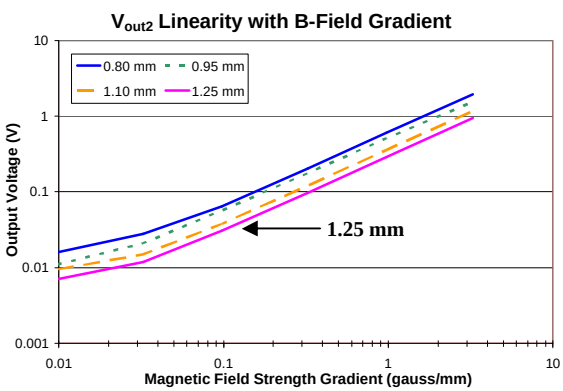

a. response by field strength

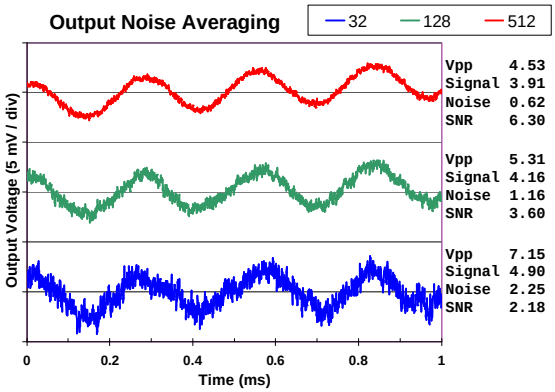

b. improving SNR by averaging

Figure IV.16 Noise Floor Experiments

When the noise bandwidth is limited to 1.95 kHz, the noise level drops to 0.62 mV which corresponds to a 2.4 Å displacement at the maximum sensitivity of the sensor. A 2.4 Å peak-to-peak motion is caused by a 2.2 nN magnitude oscillating force on a sensor with the geometry and performance of Chip E at atmospheric pressure, 760 Torr. If Q is raised to 10,000 by placing the sensor in a 2.5 mTorr vacuum, the necessary force to cause a 2.4 Å motion is 4.4 pN. This is 4.4 times larger than the 1.0 pN force caused by FDNMR requiring a 100 Hz noise bandwidth to detect the motion with a SNR of 1.

V. Conclusions and Comments

The FDNMR sensor designed, fabricated, and tested in this work successfully measures applied mechanical, acceleration, and magnetic forces by coupling the forces to electrically detected cantilever displacement. The design and fabrication goal of creating a 50 μm thick, 1 mm scale cantilever assembly which resonates at 5.0 kHz is surpassed by fabrication of two 30 μm thick cantilever sensors with resonance at 3.52 kHz and 3.63 kHz. The measured displacement sensitivity of 2.56 mV/nm for one completed sensor closely matches the expected performance of 2.70 mV/nm, demonstrating that the theoretical model of the sensor is accurate. The electrical noise floor for an SNR of 1 with an estimated 1.95 kHz noise bandwidth is measured at 0.62 mV, dictating the displacement noise floor at 2.4 Å. A 30 μm thick cantilever under vacuum moves 2.4 Å at resonance from a 4.4 pN oscillating force. The hydrogen of a 500 μm radius spherical water sample in a 1 T $\vec{B}_0$ field is predicted to generate a 1.0 pN FDNMR force, requiring a 100 Hz noise bandwidth to achieve a SNR of 1. Detecting the hydrogen sample with IDNMR and a SNR of 1 requires a 0.44 Hz noise bandwidth as the theoretical output signal using the FDNMR amplifiers is 9.2 μV. The factor of 230 increase in bandwidth and corresponding decrease in acquisition time using FDNMR confirms it as the preferred method for Micro-NMR sensing. The data further indicates that detecting hydrogen in a 0.5 T $\vec{B}_0$ field using FDNMR is feasible with a 25 Hz noise bandwidth, enabling the use of only a small permanent magnet in an embeddable Micro-NMR system.

a. Future Work

Design, fabrication, test setup, and operating condition improvements can increase the capacitive bridge sensitivity and cantilever displacement of the FDNMR sensor to increase the noise bandwidth necessary for a SNR of 1. The improved sensor can then be integrated into a Micro-NMR system for experimental measurement of the FDNMR signal from a hydrogen sample.

Design improvements can decrease C_p and C_p' and make them match and equal to 625 fF. In one approach, the abrupt transitions in Figure III.14 are minimized by extending the top aluminum layer of the sense fingers along the sense finger truss, except where the tethers secure the truss to the device edge. The

number of tethers along each finger truss is decreased from 6 to 4 and half the 60 tethers along each spring-beam are removed. The V_s and V_s' wire positions in the left and right portions of the sensor in Figure III.13b are interchanged to equalize C_p and C_p'. These changes should increase the capacitive bridge sensitivity by a factor of 1.63 to 4.17 mV/nm.

Fabrication improvements can decrease k_z and w_r, ensure reliable separation between resonant frequencies, and increase the quality factor at 760 Torr. Decreasing the thickness of the cantilever from 30 μm to 20 μm decreases k_z from 370 N/m to 100 N/m and generates more displacement from a given force. The smaller k_z also lowers w_r which more easily facilitates meeting the adiabatic condition for sample excitation by adiabatic rapid passage. Widening the 50 μm trenches in the backside etch pattern may reduce the box-canyon effect, in turn minimizing the y-direction etched surface curvature in Figure IV.4b. The resulting uniform thickness spring-beams reduces w_r relative to the torsional resonant frequency. The 0.1 μm wide stringers spanning the lateral gaps around the cantilever may cause the reduction in calculated atmospheric pressure quality factor of 430, to the experimental value of 20. Developing methods to remove these tethers and further open the lateral gaps in the structure will lower damping, improve the quality factor, and increase the motion from an oscillating force.

Test setup improvements can improve the SNR measurement by limiting the noise to bandwidth around the signal at w_r. The V_{out2} signal in this work is captured in time, averaged, and analyzed for its signal and noise components. Measuring V_{out2} with a spectrum analyzer around w_r can directly quantify SNR with a known noise bandwidth. In addition, a co-axial cable with a grounded sheath can directly connect V_{out2} from the package to the measurement equipment to shield the signal from external electromagnetic disturbances.

The V_r = ±1 V operating condition of the reference voltage that drives the bridge can be increased to ±1.5 V and maybe ±2 V and still achieve complete propagation of V_{rp} and V_{rn} to V_{bp} and V_{bn}. Pinchoff of the switch transistors limits V_r as the gate control voltage is 2.5 V. Doubling V_r has the direct impact of doubling the capacitive bridge sensitivity and reducing the input referred displacement noise floor from electronic noise by a factor of two. Combining a ±2 V V_r with the optimized C_p and C_p' would increase the capacitive bridge sensitivity by 3.26 times to 8.34 mV/nm and decreases the displacement noise floor to 0.74 Å with a 1.95 kHz

noise bandwidth. The 20 μm thick cantilever sensor requires 0.37 pN to move 0.74 Å. A bandwidth of 100 Hz reaches an SNR of 1 for the 1.0 pN FDNMR force on the optimized sensor.

b. Acknowledgements

This work received tremendous support from many individuals. My primary advisor, Dr. Gary K. Fedder was always tremendously optimistic, supportive, encouraging, patient, and financially flexible though every stage of the project. Drs. Paul J. Sides and Irving J. Oppenheim provided invaluable discussions and device mechanics analysis. Dr. Irving J. Lowe demonstrated critical expertise in understanding the fundamental physics of NMR. Dr. James A. Garrett led the team to consider FDNMR in CMOS-MEMS and remained constantly interested in all progress ranging from the physics of FDNMR to the function of the final sensor chip. Drs. James A. Bain and David N. Lambeth guided the choice of nickel as the detector magnet material. Dr. Lambeth also spent considerable time revising and commenting on this final report. Andrew Hae-Bum Yun completed significant work to compare hydrogen detection to chlorine detection by IDNMR, and Steve Wen-Chieh Lin completed the initial force and SNR computations of IDNMR and FDNMR. Many members of the CMU MEMS Laboratory provided substantial training and ideas on CMOS-MEMS processing. Mary L. Moore provided revision support and continuous gracious care to ensure the smooth completion of this work. I thank you all for your collective support of this project.

This thesis was funded by three organizations. The National Science Foundation provided funds though the XYZ-on-a-Chip project, under grant CMS-9980759. The Defense Advanced Research Projects Agency supported this work through the Application Specific Integrated Multiuser Process Service at Carnegie Mellon University. Northrop Grumman Corporation contributed to this work by providing a Northrop Grumman Fellowship. The multiple sources of support were essential to allow the financial flexibility necessary to complete this project.

VI. References

[1] B. A. M. Anderson, O. Hansen, and M. Kristensen. "Spatial Variation of the Etch Rate for Deep Etching of Silicon by Reactive Ion Etching." *Journal of Vacuum Science Technology B*, Vol. 15, No. 4, pp. 993-999. 1997.

[2] Austria MicroSystems AG, A 8141 Schloss, Premstätten, Austria. www.austriamicrosystems.com

[3] F. Ayazi and K. Najafi. "High Aspect-Ratio Combined Poly and Single-Crystal Silicon (HARPSS) MEMS Technology." *Journal of Microelectromechanical Systems*, Vol. 9, No. 3, pp. 288-294. 2000.

[4] A. A. Ayón, X. Zhang, and R. Khanna. "Anisotropic Silicon Trenches 300-500 μm Deep Employing Time Multiplexed Deep Etching (TDME)." *Sensors and Actuators A*, Vol 91, pp. 381-385. 2001.

[5] A. A. Ayón, R. A. Braff, C. C. Lin, H. H. Sawin, and M. A. Schmidt. "Characterization of a Time Multiplexed Inductively Coupled Plasma Etcher." *Journal of the Electrochemical Society*, Vol. 146, No. 1, pp. 339-349. 1999.

[6] A. A. Ayón, K. Ishihara, R. A. Braff, H. H. Sawin, and M. A. Schmidt. "Application of the Footing Effect in the Micromachining of Self-Aligned, Free-Standing, Complimentary Metal–Oxide–Semiconductor Compatible Structures." *Journal of Vacuum Science Technology* A, Vol. 17, No. 4, pp. 2274-2279. 1999.

[7] G. Boero. *Integrated NMR Probe for Magnetometry*. PhD Thesis No. 2211, Department of Microengineering, École Polytechnique Fédèrale de Lausanne, Lausanne, Switzerland. 2000.

[8] K. J. Bruland, W. M. Dougherty, J. L. Garbini, J. A. Sidles, and S. H. Chao. "Force-detected Magnetic Resonance in a Field Gradient of 2500,000 Tesla per Meter." *Applied Physics Letters*, Vol. 73, No. 21, pp. 3159-3161. 1998.

[9] D. Canet. *Nuclear Magnetic Resonance*. John Wiley & Sons, West Sussex. 1996.

[10] K.-S. Chen, A. A. Ayón, X. Zhang, and S. M. Spearing. "Effect of Process Paramenters on the Surface Morphology and Mechanical Performance of Silicon Structures After Deep Reactive Ion Etching (DRIE)." *Journal of Microelectromechanical Systems*, Vol. 11, No. 3, pp. 264-275. 2002.

[11] W. Chieh and G. K Fedder. "A Comparison of Induction-Detection NMR and Force-Detection NMR on Micro-NMR Device Design." The Robotics Institute, Carnegie Mellon University, Report CMU-RI-TR-01-06. 2001.

[12] COMSOL, 8 New England Executive Park, Suite 310, Burlington, MA 01803. www.comsol.com

[13] Coventor, 4001 Weston Parkway, Cary, NC 27513. www.coventor.com

[14] W. J. Dauksher, S. B. Clemens, D. J. Resnick, K. H. Smith, P. J, S. Mangat, S. Rauf, P. L. G. Vantzek, H. Ashraf, L. Lea, S. Hall, I. R. Johnston, J. Hopkins, A. Chambers, and J. K. Bhardwaj. "Modeling and Development of a Deep Silicon Etch Process for 200 mm Electron Projection Lithography Mask Fabrication." *Journal of Vacuum Science Technology B,* Vol 19, No. 6, pp. 2921-2925. 2001.

[15] G. K. Fedder. *Simulation of Microelectromechanical Systems*. PhD Thesis, Department of Electrical Engineering and Computer Sciences, University of California, Berkley, California. 1994.

[16] G. K. Fedder, S. Santhanam, M. L. Reed, S. C. Eagle, D. F. Guillou, M. S.-C. Lu, and L. R. Carley. "Laminated High-Aspect-Ratio Microstructures in a Conventional CMOS Process." Proceedings of the 9th IEEE International Workshop on Micro Electro Mechanical Systems, pp 13-18. 1996.

[17] D. Gadian. *NMR and its Applications to Living Systems*. Oxford University Press, New York. 1995.

[18] J. H. Garrett, G. K. Fedder, K. M. Frederick, J.-J. Hsu, I. J. Lowe, I. J. Oppenheim, M. E. Patton, P. J. Sides, and H. A. Yun. "Developments in Chlorine Detection in Concrete using NMR," SPIE Smart Structures Conference SS05: Systems for Bridges, Structures, and Highways. 2002.

[19] General Electric Company, 3135 Easton Turnpike, Fairfield, Connecticut, USA. www.ge.com

[20] D. N. Grant and R. K. Harris. *Encyclopedia of Nuclear Magnetic Resonance, Volume 1, Historical Perspectives*. John Wiley & Sons, West Sussex. 2002.

[21] D. I. Hoult and R. E. Richards. "The Signal-to-Noise Ratio of the Nuclear Magnetic Resonance." *Journal of Magnetic Resonance*, Vol. 24, pp. 71-85. 1976.

[22] F. Laermer and A. Schilp of Robert Bosch GmbH. "Method of Anisotropically Etching Silicon." United States Patent No. 5501893. 1996.

[23] H. Lakdawala. *Temperature Control of CMOS Micromachined Sensors*. PhD Thesis, Department of Electrical and Computer Engineering, Carnegie Mellon University, Pittsburgh, Pennsylvania. 2002.

[24] G. M. Leskowitz, L. A. Madsen, and D. P. Weitekamp. "Force-Detected Magnetic Resonance Without Field Gradients." *Solid State Nuclear Magnetic Resonance*, Vol. 11, pp. 73-86. 1998.

[25] S. Liebert. "Encapsulation of Naked Dies for Bulk Silicon Etching with TMAH." *Microelectronics Reliability*, Vol. 42, pp.1939-1944. 2002.

[26] The MOSIS Service, 4676 Admiralty Way, Marina del Rey, California, USA. www.mosis.org

[27] M. Ohring. *The Materials Science of Thin Films*. Academic Press, San Diego. 1992.

[28] T. L. Peck, R. L. Magin, and P. L. Lauterbur. "Design and Analysis of Microcoils for NMR Microscopy." *Journal of Magnetic Resonance B*, Vol. 108, pp. 114-124. 1995.

[29] Protasis: Magnetic Resonance Microsensors. 101 Tomaras Avenue, Savoy, IL. www.protasis.com

[30] D. Rugar, O. Züger, S. Hoen, C. S. Yannoni, H.-M. Vieth, and R. D. Kendrick. "Force Detection of Nuclear Magnetic Resonance." *Science*, Vol. 264, pp. 1560-1563. 1994.

[31] K. A. Shaw, Z. L. Zhang, and N. C. MacDonald. "SCREAM-I: A Single Mask, Single-Crystal Silicon, Reactive Ion Process for Microelectromechanical Structures." *Sensors and Actuators A*, Vol. 40, No. 1, pp. 63-70. 1994.

[32] J. A. Sidles. "Noninductive Detection of Single-Proton Magnetic Resonance." *Applied Physics Letters*, Vol. 58, No. 24, pp. 2854-2856. 1991.

[33] J. E. Stocker, T. L. Peck, A. G. Webb, M. Feng, and R. L. Magin. "Nanoliter Volume, High-Resolution NMR Microspectroscopy Using 60-μm Planar Microcoil." IEEE Transactions on Biomedical Engineering, Vol. 44, No. 11, pp. 1122-1126. 1997.

[34] T. Veijola, H.Kuisma, J. Lahdenperä, and T. Ryhänen.. "Equivalent-Circuit Model of the Squeezed Gas Film in a Silicon Accelerometer." *Sensors and Actuators A*, Vol. 48, pp. 239-248. 1995.

[35] K. Wago, D. Botkin, C. S. Yannoni, and D. Rugar. "Force-Detected Electron-Spin Resonance: Adiabatic Inversion, Nutation, and Spin Echo." *Physical Review B*, Vol. 57, No. 2, pp. 1108-1114. 1998.

[36] H. Xie, L. Erdmann, X. Zhu, K. J. Gabriel, and G. K. Fedder. "Post-CMOS Processing for High-Aspect-Ratio Integrated Silicon Microstructures." *Journal of Microelectromechanical Systems*, Vol. 11, No. 2, pp. 93-101. 2002.

[37] H. Xie, and G. K. Fedder. "Vertical Comb-Finger Capacitive Actuation and Sensing for CMOS-MEMS." *Sensors and Actuators A: Physical*, Vol. 95, pp. 212-221. 2002.

[38] H. A. Yun, M. E. Patton, J. H. Garrett, G. K. Fedder, K. M. Frederick, J.-J. Hsu, I. J. Lowe, I. J. Oppenheim, and P. J. Sides. "Detection of Free Chloride in Concentrate by NMR." *Cement and Concrete Research, an International Journal.* 2003.

[39] X. Zhu. *Post-CMOS Micromachining of Surface and Bulk Structures*. PhD Thesis, Department of Electrical and Computer Engineering, Carnegie Mellon University, Pittsburgh, Pennsylvania. 2002.